Constraints on Southern Ocean Shortwave Cloud Feedback from the Hydrological Cycle

Chuyan Tan[1], Daniel Thompson McCoy[1], and Gregory Elsaesser[2]

[1]University of Wyoming
[2]Columbia University APAM/NASA GISS

December 3, 2023

Abstract

Shifts in Southern Ocean (SO, $40 - 85^{o}S$) shortwave cloud feedback (SW_{FB}) toward more positive values are the dominant contributor to higher effective climate sensitivity (ECS) in Coupled Model Intercomparison Project phase 6 (CMIP6) models. To provide an observational constraint on the SO SW_{FB}, we use a simplified physical model to connect SO SW_{FB} with the response of column-integrated liquid water mass (LWP) to warming and the susceptibility of albedo to LWP in 50 CMIP5 and CMIP6 GCMs. In turn, we predict the responses of SO LWP using a cloud-controlling factor (CCF) model. The combination of the CCF model and radiative susceptibility explains about 50\% of the variance in the GCM-simulated SW_{FB} in the SO. Observations of SW radiation fluxes, LWP, and CCFs from reanalysis are used to constrain the SO SW_{FB}. The response of SO LWP to warming is constrained to $2.76\ -\ 4.19$ $g\ m^{-2}\ K^{-1}$, relative to a GCM prior of $0.64\ -\ 9.33$ $g\ m^{-2}\ K^{-1}$. The susceptibility of albedo to LWP is constrained to be $0.43\ -\ 0.90$ $ (kg\ m^{-2})^{-1}$, relative to $0.30\ -\ 3.91$ $(kg\ m^{-2})^{-1}$. The overall constraint on the contribution of SO to global mean SW_{FB} is $-0.168\ -\ 0.051$ $W\ m^{-2}\ K^{-1}$, relative to $-0.277\ -\ 0.270$ $ W m^{-2} K^{-1}$. In summary, observations suggest SO SW_{FB} is less likely to be as extremely positive as predicted by some CMIP6 GCMs, but more likely to range from moderate negative to weakly positive.

Relationships between SW_{FB}, LWP Response ($\frac{\Delta LWP}{\Delta GMT}$), and Climate Sensitivity

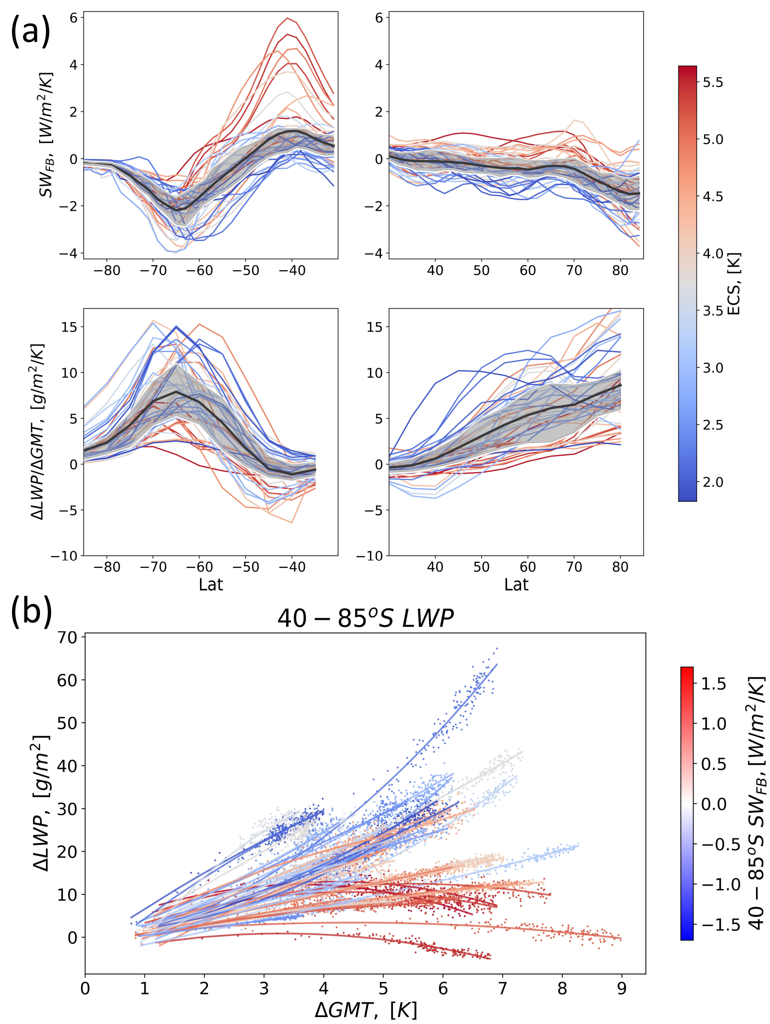

Prediction of Observed LWP

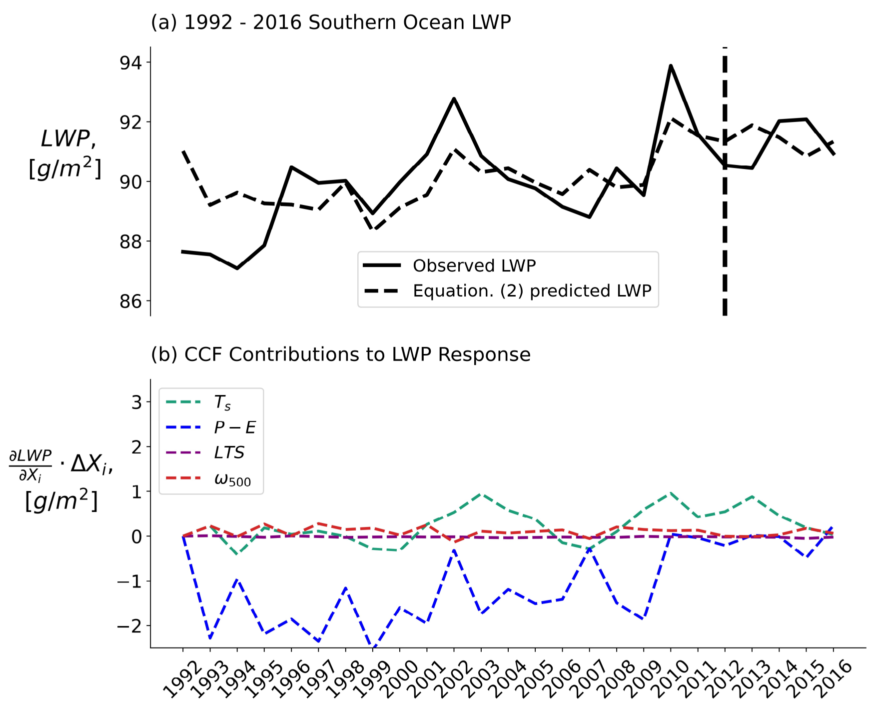

Constraints on GCM LWP Response $\left(\frac{\Delta \mathrm{LWP}}{\Delta \mathrm{GMT}}\right)$

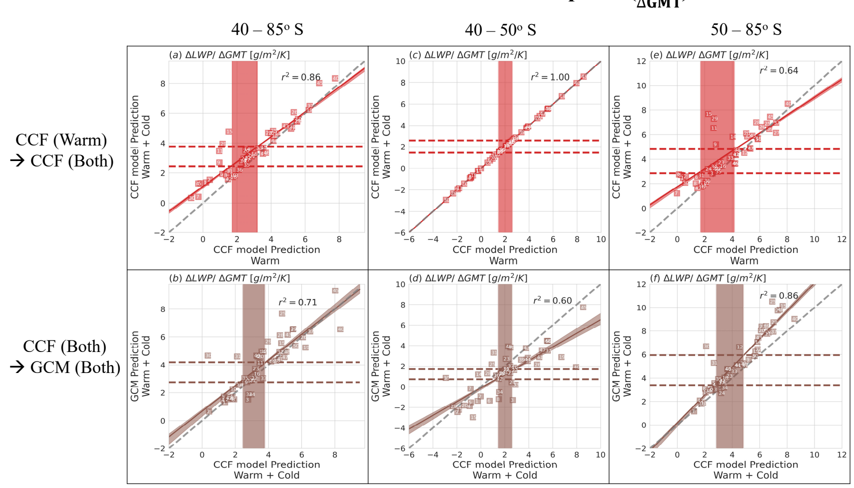

Decomposition on LWP Response ($\frac{\Delta \mathrm{LWP}}{\Delta \mathrm{GMT}}$)

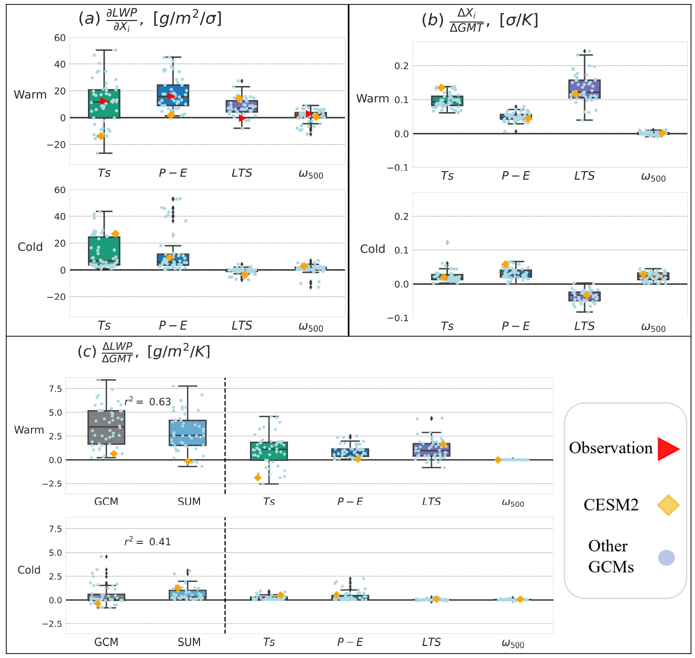

Constraint on Radiative Susceptibility ($\frac{\partial \alpha}{\partial \mathrm{LWP}}$)

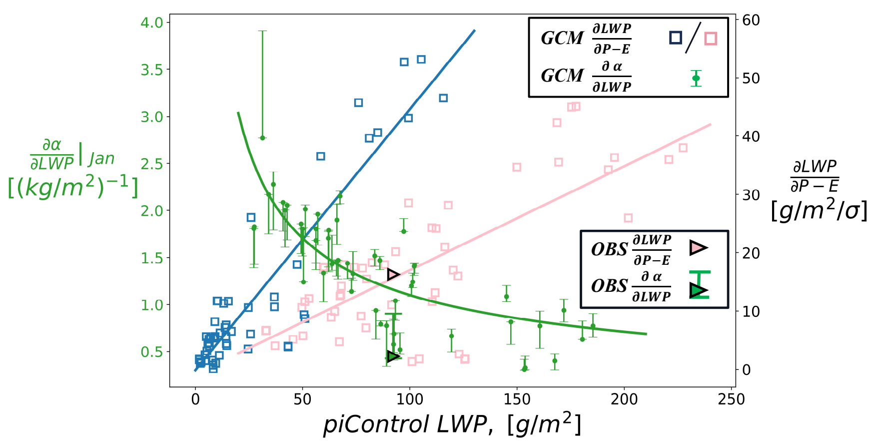

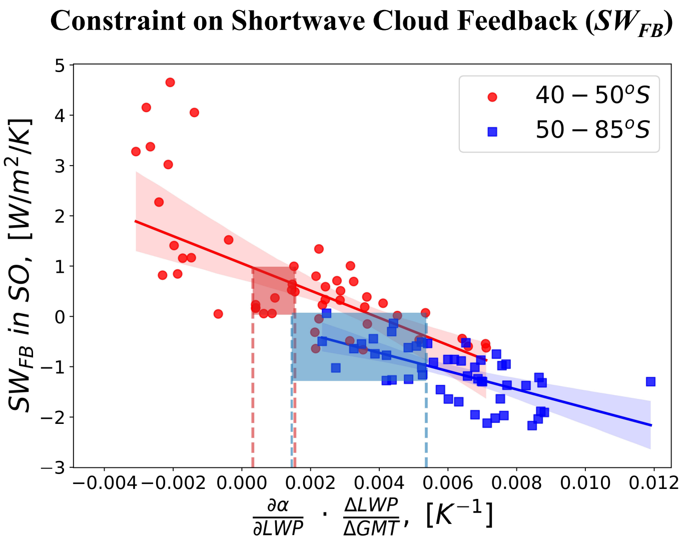
Constraint on Shortwave Cloud Feedback (SW_{FB})
$40-50^oS$
$50-85^oS$
SW_{FB} in SO, $[W/m^2/K]$
$\frac{\partial\alpha}{\partial LWP}\cdot\frac{\Delta LWP}{\Delta GMT}$, $[K^{-1}]$

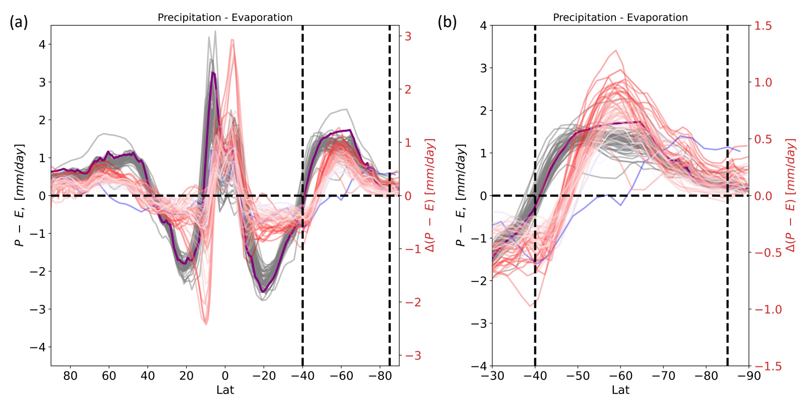
(a)
Precipitation - Evaporation
$P-E$, $[mm/day]$
$\Delta(P-E)$ $[mm/day]$
Lat
(b)
Precipitation - Evaporation
$P-E$, $[mm/day]$
$\Delta(P-E)$ $[mm/day]$
Lat

Prediction of Observed LWP

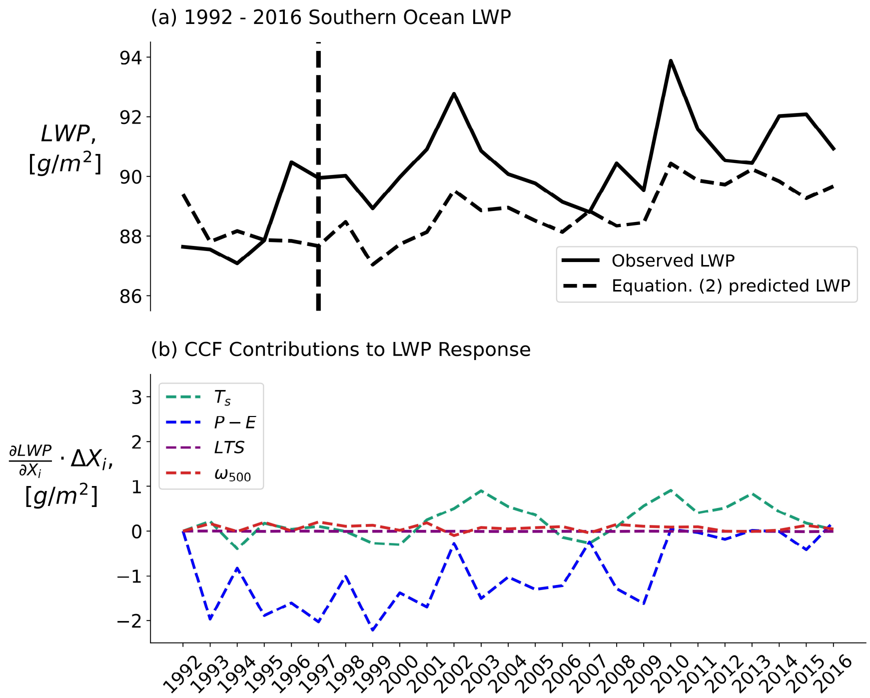

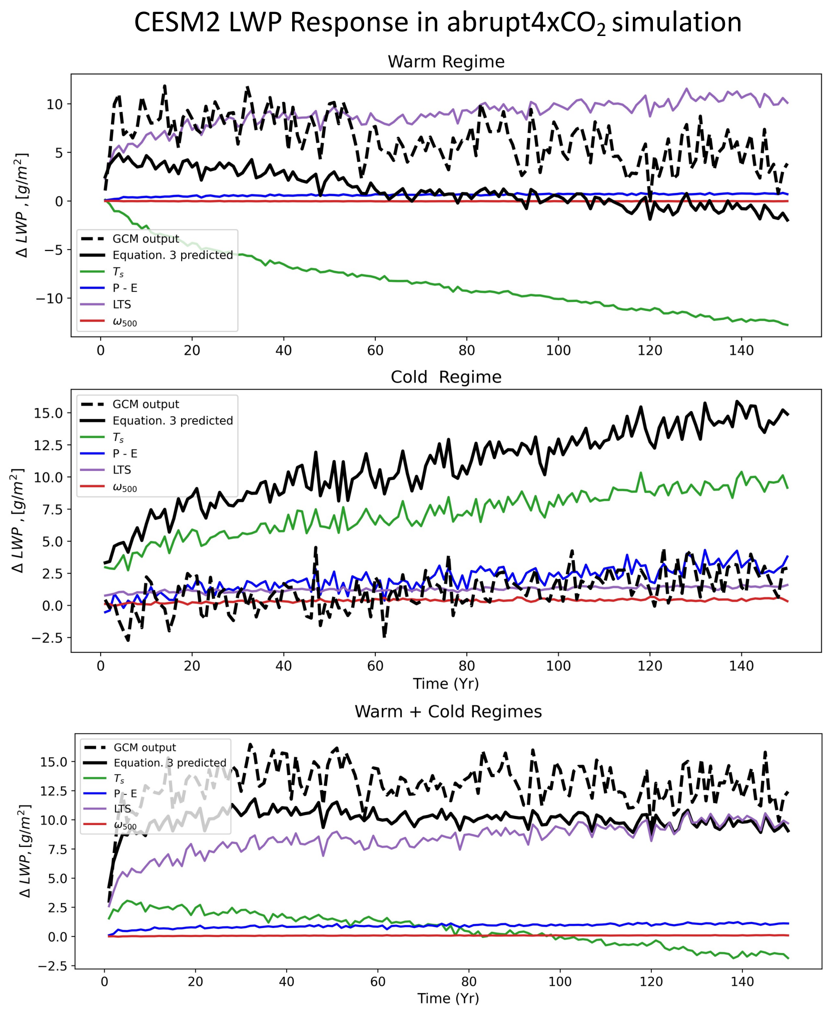
CESM2 LWP Response in abrupt4xCO$_2$ simulation
Warm Regime
Cold Regime
Warm + Cold Regimes
GCM output
Equation. 3 predicted
T_s
P - E
LTS
ω_{500}
Δ LWP , $[g/m^2]$
Time (Yr)

Responses of LWP to P–E in GCM abrupt4xCO_2 simulations

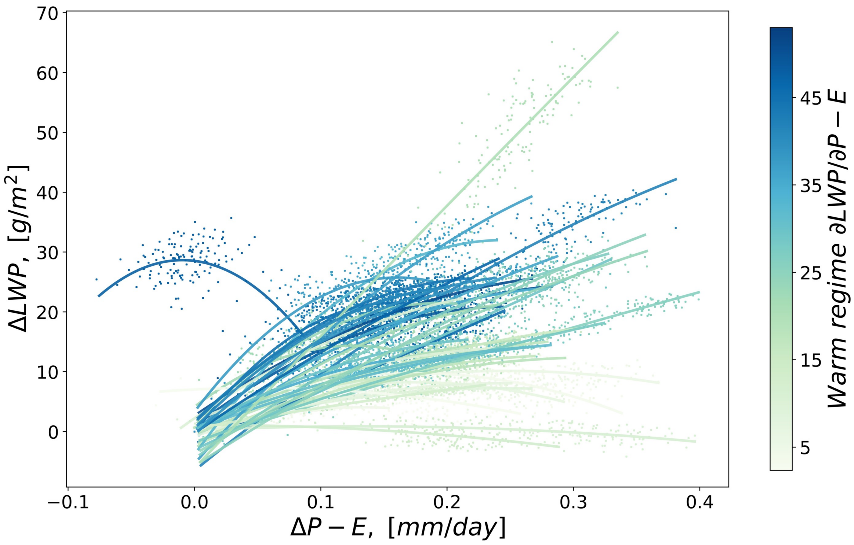

Contributions of LWP & IWP to Albedo (α) Changes in the SO

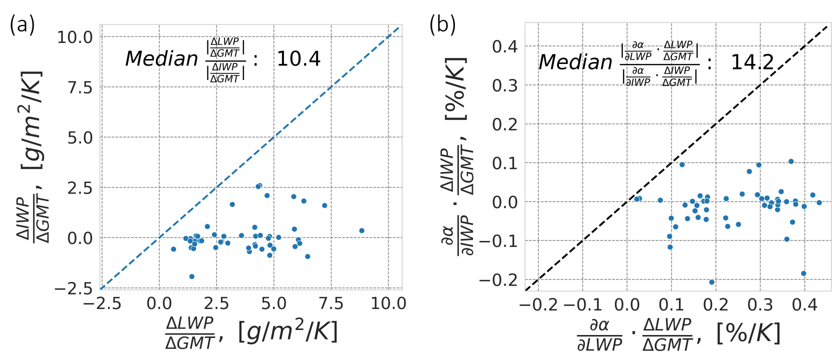

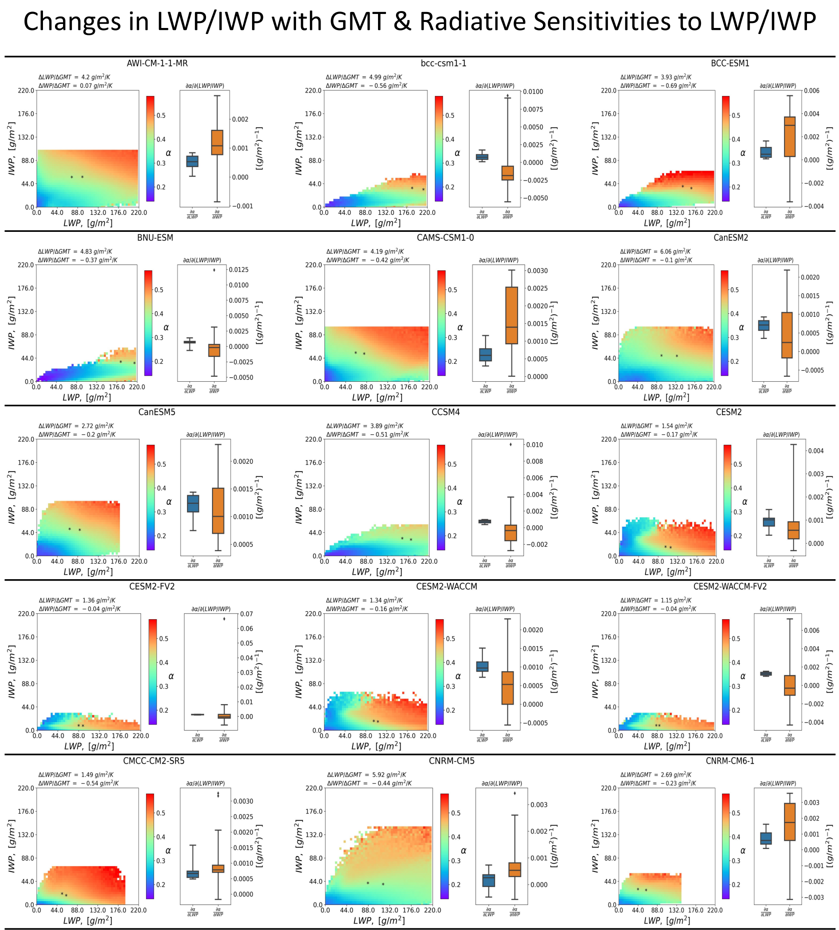
Changes in LWP/IWP with GMT & Radiative Sensitivities to LWP/IWP
AWI-CM-1-1-MR
bcc-csm1-1
BCC-ESM1
BNU-ESM
CAMS-CSM1-0
CanESM2
CanESM5
CCSM4
CESM2
CESM2-FV2
CESM2-WACCM
CESM2-WACCM-FV2
CMCC-CM2-SR5
CNRM-CM5
CNRM-CM6-1

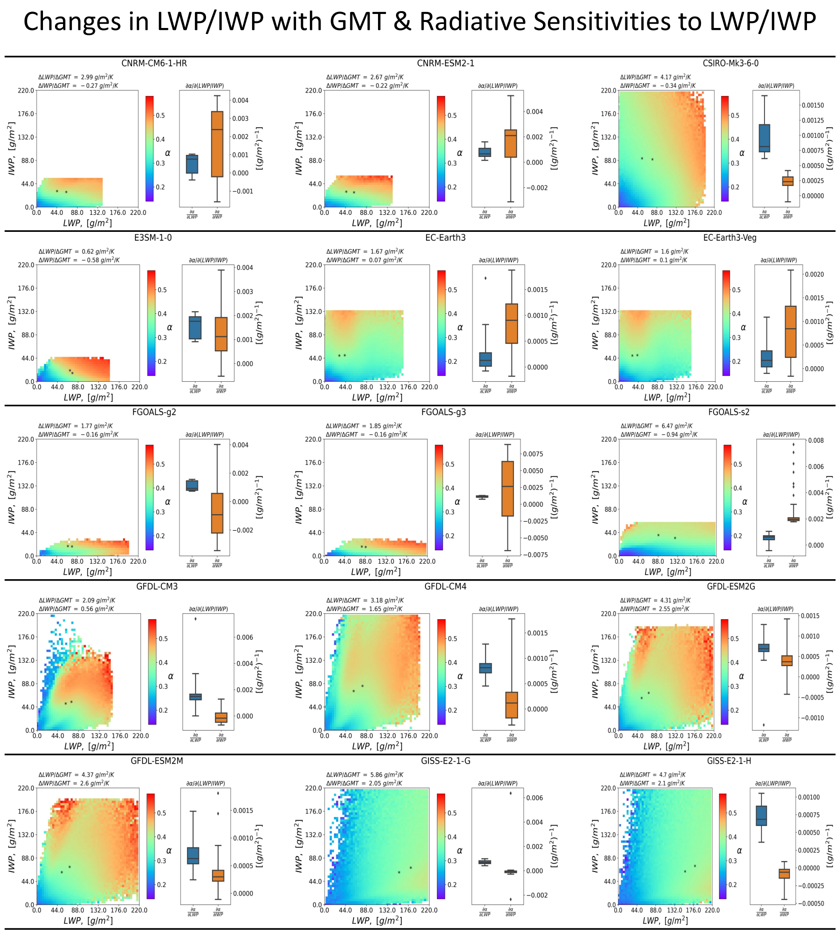
Changes in LWP/IWP with GMT & Radiative Sensitivities to LWP/IWP
CNRM-CM6-1-HR
CNRM-ESM2-1
CSIRO-Mk3-6-0
E3SM-1-0
EC-Earth3
EC-Earth3-Veg
FGOALS-g2
FGOALS-g3
FGOALS-s2
GFDL-CM3
GFDL-CM4
GFDL-ESM2G
GFDL-ESM2M
GISS-E2-1-G
GISS-E2-1-H

Changes in LWP/IWP with GMT & Radiative Sensitivities to LWP/IWP

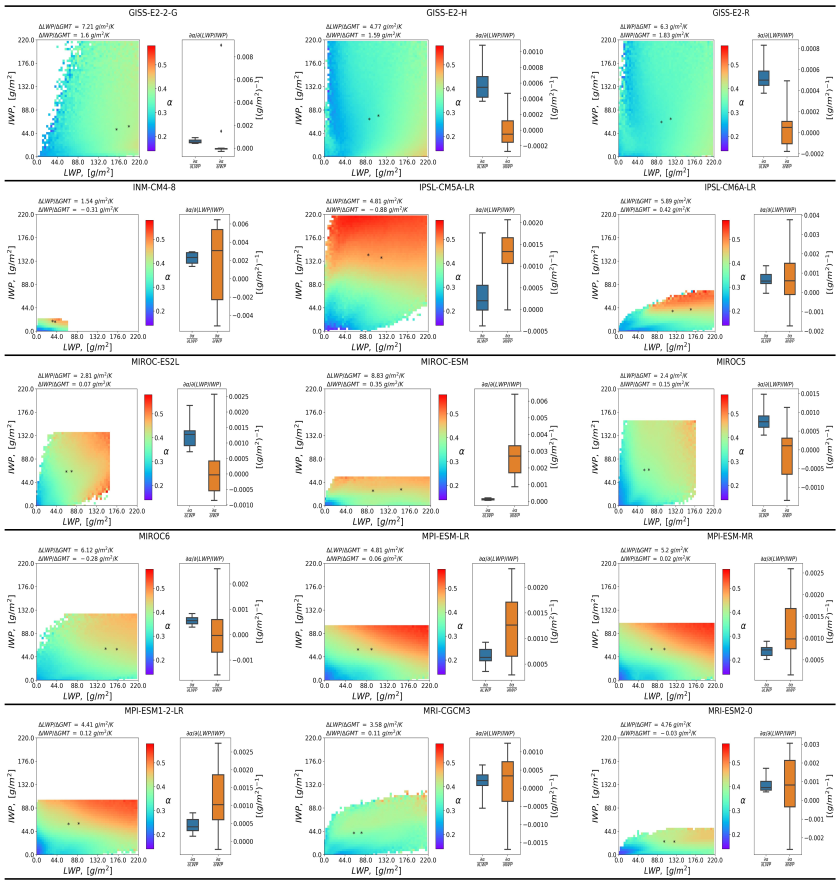

Changes in LWP/IWP with GMT & Radiative Sensitivities to LWP/IWP

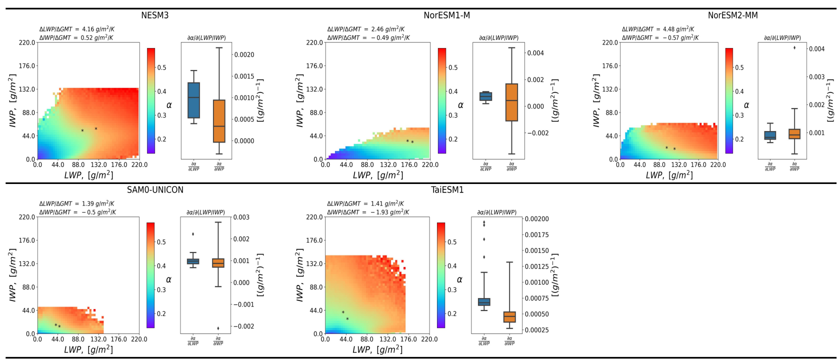

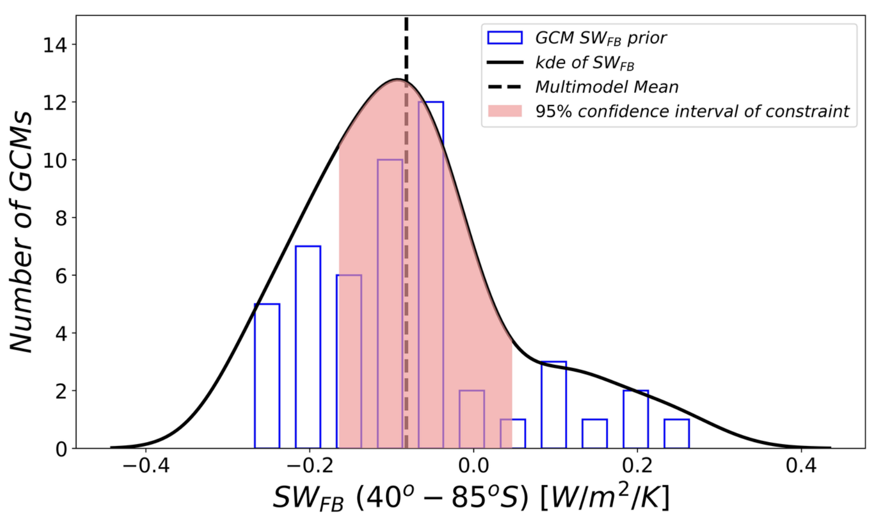

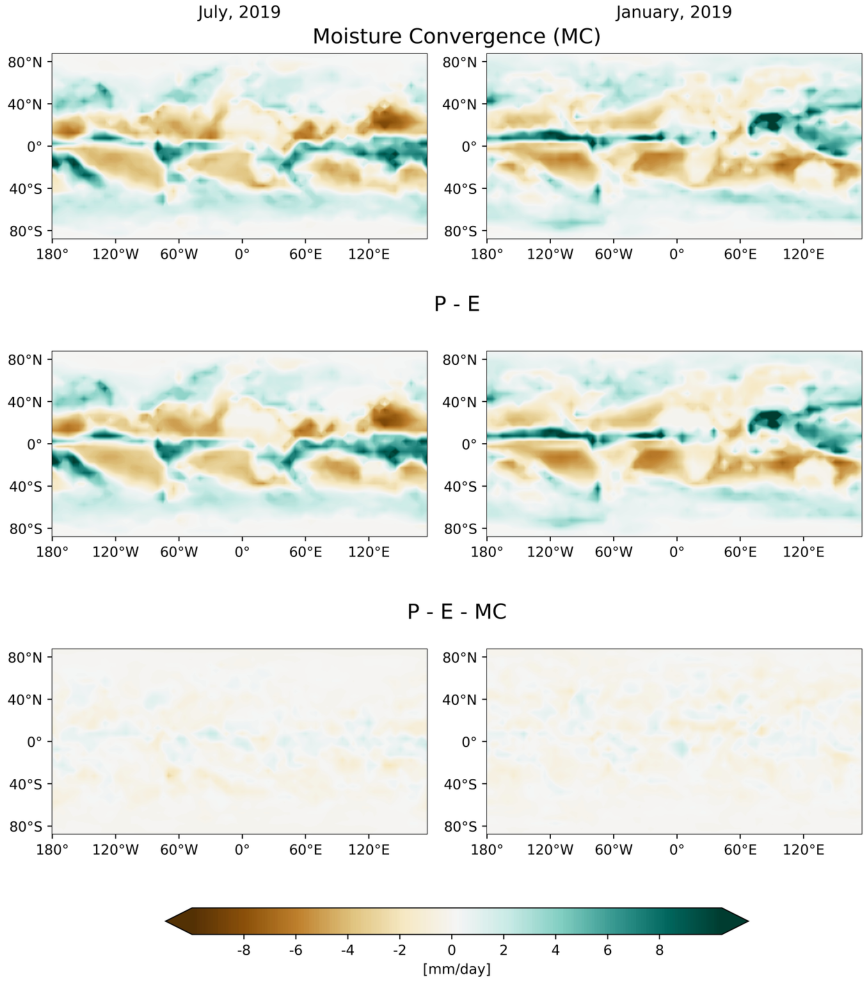

July, 2019
January, 2019
Moisture Convergence (MC)
P - E
P - E - MC
80°N
40°N
0°
40°S
80°S
180°
120°W
60°W
0°
60°E
120°E
-8
-6
-4
-2
0
2
4
6
8
[mm/day]

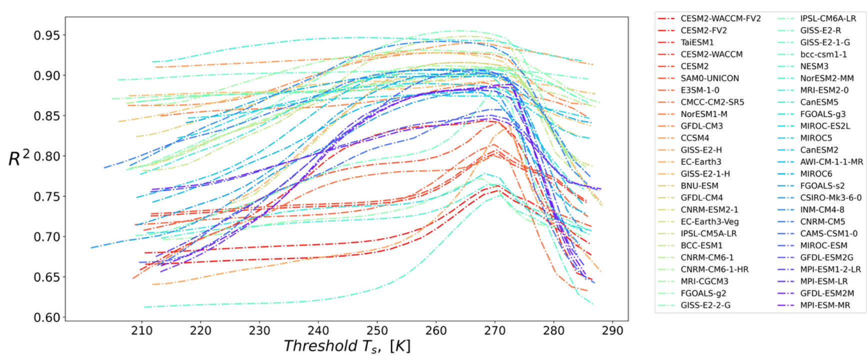

R^2
0.95
0.90
0.85
0.80
0.75
0.70
0.65
0.60
210
220
230
240
250
260
270
280
290
Threshold T_s, [K]
CESM2-WACCM-FV2
CESM2-FV2
TaiESM1
CESM2-WACCM
CESM2
SAM0-UNICON
E3SM-1-0
CMCC-CM2-SR5
NorESM1-M
GFDL-CM3
CCSM4
GISS-E2-H
EC-Earth3
GISS-E2-1-H
BNU-ESM
GFDL-CM4
CNRM-ESM2-1
EC-Earth3-Veg
IPSL-CM5A-LR
BCC-ESM1
CNRM-CM6-1
CNRM-CM6-1-HR
MRI-CGCM3
FGOALS-g2
GISS-E2-2-G
IPSL-CM6A-LR
GISS-E2-R
GISS-E2-1-G
bcc-csm1-1
NESM3
NorESM2-MM
MRI-ESM2-0
CanESM5
FGOALS-g3
MIROC-ES2L
MIROC5
CanESM2
AWI-CM-1-1-MR
MIROC6
FGOALS-s2
CSIRO-Mk3-6-0
INM-CM4-8
CNRM-CM5
CAMS-CSM1-0
MIROC-ESM
GFDL-ESM2G
MPI-ESM1-2-LR
MPI-ESM-LR
GFDL-ESM2M
MPI-ESM-MR

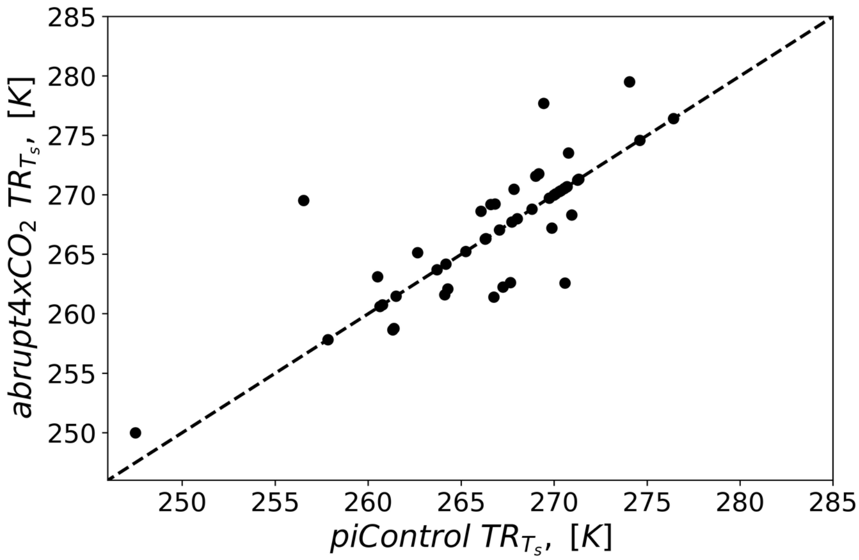

abrupt4xCO2 TR_Ts', [K]
piControl TR_Ts, [K]
250
255
260
265
270
275
280
285

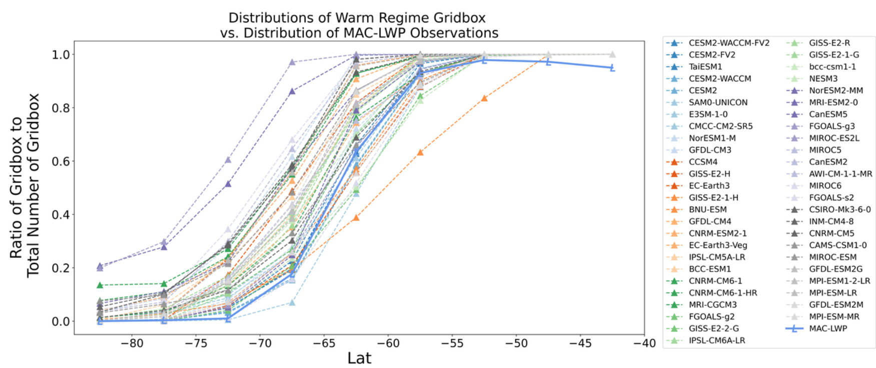

Distributions of Warm Regime Gridbox
vs. Distribution of MAC-LWP Observations
Ratio of Gridbox to
Total Number of Gridbox
Lat
CESM2-WACCM-FV2
CESM2-FV2
TaiESM1
CESM2-WACCM
CESM2
SAM0-UNICON
E3SM-1-0
CMCC-CM2-SR5
NorESM1-M
GFDL-CM3
CCSM4
GISS-E2-H
EC-Earth3
GISS-E2-1-H
BNU-ESM
GFDL-CM4
CNRM-ESM2-1
EC-Earth3-Veg
IPSL-CM5A-LR
BCC-ESM1
CNRM-CM6-1
CNRM-CM6-1-HR
MRI-CGCM3
FGOALS-g2
GISS-E2-2-G
IPSL-CM6A-LR
GISS-E2-R
GISS-E2-1-G
bcc-csm1-1
NESM3
NorESM2-MM
MRI-ESM2-0
CanESM5
FGOALS-g3
MIROC-ES2L
MIROC5
CanESM2
AWI-CM-1-1-MR
MIROC6
FGOALS-s2
CSIRO-Mk3-6-0
INM-CM4-8
CNRM-CM5
CAMS-CSM1-0
MIROC-ESM
GFDL-ESM2G
MPI-ESM1-2-LR
MPI-ESM-LR
GFDL-ESM2M
MPI-ESM-MR
MAC-LWP

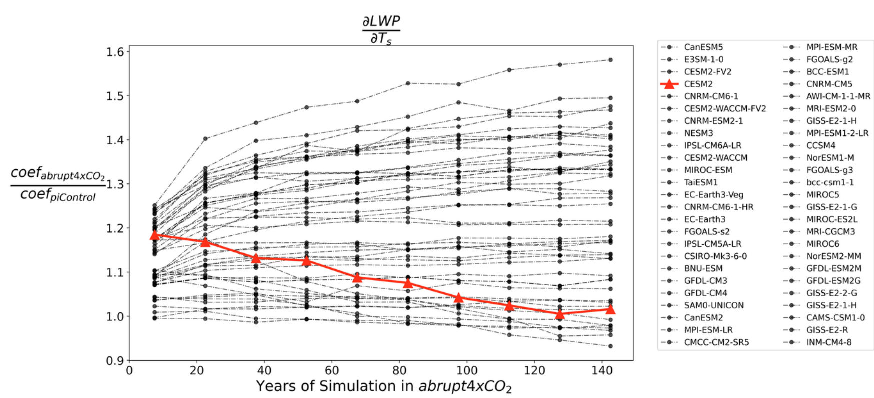

∂LWP/∂T_s
coef_abrupt4xCO2 / coef_piControl
Years of Simulation in abrupt4xCO2
CanESM5
E3SM-1-0
CESM2-FV2
CESM2
CNRM-CM6-1
CESM2-WACCM-FV2
CNRM-ESM2-1
NESM3
IPSL-CM6A-LR
CESM2-WACCM
MIROC-ESM
TaiESM1
EC-Earth3-Veg
CNRM-CM6-1-HR
EC-Earth3
FGOALS-s2
IPSL-CM5A-LR
CSIRO-Mk3-6-0
BNU-ESM
GFDL-CM3
GFDL-CM4
SAM0-UNICON
CanESM2
MPI-ESM-LR
CMCC-CM2-SR5
MPI-ESM-MR
FGOALS-g2
BCC-ESM1
CNRM-CM5
AWI-CM-1-1-MR
MRI-ESM2-0
GISS-E2-1-H
MPI-ESM1-2-LR
CCSM4
NorESM1-M
FGOALS-g3
bcc-csm1-1
MIROC5
GISS-E2-1-G
MIROC-ES2L
MRI-CGCM3
MIROC6
NorESM2-MM
GFDL-ESM2M
GFDL-ESM2G
GISS-E2-2-G
GISS-E2-1-H
CAMS-CSM1-0
GISS-E2-R
INM-CM4-8

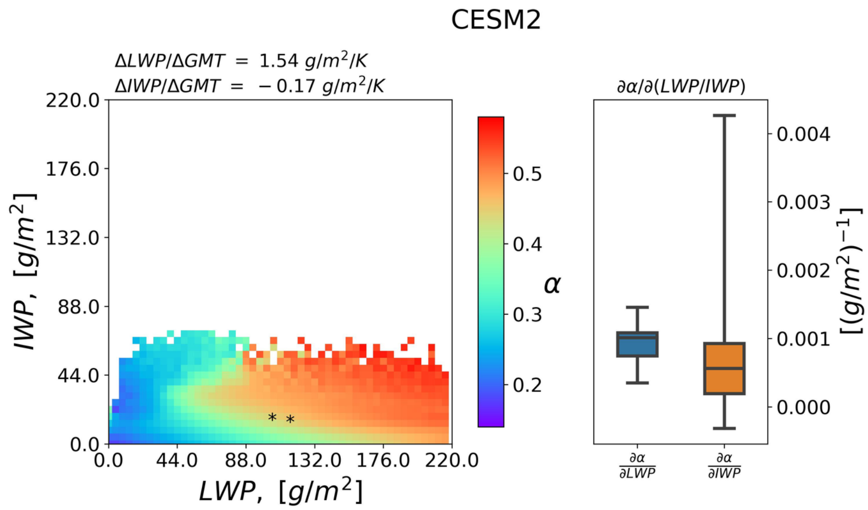

CESM2
$\Delta LWP/\Delta GMT\ =\ 1.54\ g/m^2/K$
$\Delta IWP/\Delta GMT\ =\ -0.17\ g/m^2/K$
220.0
176.0
132.0
88.0
44.0
0.0
$IWP,\ [g/m^2]$
0.0
44.0
88.0
132.0
176.0
220.0
$LWP,\ [g/m^2]$
0.5
0.4
0.3
0.2
α
$\partial\alpha/\partial(LWP/IWP)$
0.004
0.003
0.002
0.001
0.000
$[(g/m^2)^{-1}]$
$\frac{\partial\alpha}{\partial LWP}$
$\frac{\partial\alpha}{\partial IWP}$

Constraints on Southern Ocean Shortwave Cloud Feedback from the Hydrological Cycle

Chuyan Tan[1*], Daniel T. McCoy[1], Gregory S. Elsaesser[2,3]

[1]University of Wyoming, Laramie, WY, USA
[2]Columbia University, Dept. of Appl. Physics and Appl. Mathematics, New York, NY, USA
[3]NASA Goddard Institute for Space Studies (GISS), New York, NY, USA
[*]Now at: Hunan Climate Center, Changsha, China

Key Points:

- Southern Ocean liquid water path increased over the past two decades due to enhanced moisture convergence.
- Enhanced moisture convergence contributes to a negative cloud feedback in the Southern Ocean.
- Across global climate models, the sensitivity of upwelling shortwave to cloud opposes the sensitivity of cloud to moisture convergence.

Corresponding author: D. T. McCoy, `daniel.mccoy@uwyo.edu`

Abstract

Shifts in Southern Ocean (SO, $40-85^oS$) shortwave cloud feedback (SW_{FB}) toward more positive values are the dominant contributor to higher effective climate sensitivity (ECS) in Coupled Model Intercomparison Project phase 6 (CMIP6) models. To provide an observational constraint on the SO SW_{FB}, we use a simplified physical model to connect SO SW_{FB} with the response of column-integrated liquid water mass (LWP) to warming and the susceptibility of albedo to LWP in 50 CMIP5 and CMIP6 GCMs. In turn, we predict the responses of SO LWP using a cloud-controlling factor (CCF) model. The combination of the CCF model and radiative susceptibility explains about 50% of the variance in the GCM-simulated SW_{FB} in the SO. Observations of SW radiation fluxes, LWP, and CCFs from reanalysis are used to constrain the SO SW_{FB}. The response of SO LWP to warming is constrained to $2.76-4.19\ g\ m^{-2}\ K^{-1}$, relative to a GCM prior of $0.64\ -\ 9.33\ g\ m^{-2}\ K^{-1}$. The susceptibility of albedo to LWP is constrained to be $0.43\ -\ 0.90\ (kg\ m^{-2})^{-1}$, relative to $0.30\ -\ 3.91\ (kg\ m^{-2})^{-1}$. The overall constraint on the contribution of SO to global mean SW_{FB} is $-0.168-0.051\ W\ m^{-2}\ K^{-1}$, relative to $-0.277\ -\ 0.270\ Wm^{-2}K^{-1}$. In summary, observations suggest SO SW_{FB} is less likely to be as extremely positive as predicted by some CMIP6 GCMs, but more likely to range from moderate negative to weakly positive.

Plain Language Summary

Previous studies suggest that SO clouds reflect more sunlight in response to global warming and more strongly cool the planet - a negative shortwave cloud feedback (SW_{FB}). The SO SW_{FB} in the latest generation of global climate models (GCMs) participating in the Coupled Model Intercomparison Project phase 6 (CMIP6) has shifted toward more positive values, leading to the larger predicted temperature responses to greenhouse gas increases in these GCMs. In this study, we examine if this more positive SW_{FB} is consistent with observations. We connect the effect of SO clouds on reflected sunlight with the predicted response of cloud liquid content to global warming. The linkage between cloud liquid water content and large-scale meteorology is applied to predict this cloud liquid response. Satellite observations of reflected sunlight, cloud liquid, and observations of large-scale meteorology are applied to constrain the SO SW_{FB} for 50 CMIP5 and CMIP6 GCMs. The results suggest that SO cloud liquid will increase with warming around the average of predictions of 50 GCMs. Satellite records suggest that the sensitivity of reflected sunlight to cloud liquid is weak compared to GCMs. In combination, our results suggest SO clouds most likely reflect more sunlight back to space and further cool our planet.

1 Introduction

Quantifying the surface temperature response to a doubling in atmospheric CO_2 concentration, commonly referred to as climate sensitivity, is a fundamental goal of climate science (Houghton & el., 2001; Boucher & el., 2014; Forster & el., 2023). Climate feedback processes such as changes in lapse rate, water vapor, and cloud may dampen or amplify the temperature response to greenhouse gas increase and are critical for estimating climate sensitivity (Bony et al., 2006). Global climate models (GCMs) provide the most direct way to estimate climate sensitivity since they attempt to simulate all relevant processes, including climate feedback (Andrews et al., 2012; Zelinka, Myers, McCoy, Po-Chedley, et al., 2020). Shortwave cloud feedback (SW_{FB}), the shortwave (SW) radiative impact of cloud responses to a surface temperature perturbation, is the largest uncertainty in GCMs' estimate of net climate feedback and by extension, climate sensitivity (Zelinka, Myers, McCoy, Po-Chedley, et al., 2020; Sherwood et al., 2020). The uncertainty in estimating SW_{FB} is strongly driven by difficulties in representing subgrid-scale cloud processes in GCMs (Storelvmo et al., 2015; Webb et al., 2015; Sherwood et al., 2014; Zhao, 2014).

Despite the large intermodel spread in global-mean SW_{FB}, robust regional features have emerged from previous generations of GCMs. For example, positive SW_{FB} in the subtropics has emerged, likely due to decreased cloud coverage with negative SW_{FB} in the middle-to-high latitudes likely attributed to increased cloud optical depth (Zelinka et al., 2012; Ceppi, McCoy, & Hartmann, 2016). Considerable progress has been made on narrowing the possible ranges of tropical and subtropical SW_{FB} using observational constraints (Myers et al., 2021; G. V. Cesana & Del Genio, 2021; G. Cesana et al., 2019; Scott et al., 2020; Klein et al., 2017).

Recent GCMs have suggested a weaker negative Southern Ocean (SO, $40-85^oS$) SW_{FB}. The ensemble mean SO SW_{FB} of GCMs participating in the sixth phase of the Coupled Model Intercomparison Project (CMIP6) has shifted toward a more positive value relative to CMIP5, leading to the emergence of several GCMs with high effective climate sensitivity (ECS) (ECS $\geq$ 4.5K) (Zelinka, Myers, McCoy, Po-Chedley, et al., 2020; Bodas-Salcedo et al., 2019). Much effort has been made to understand this change within the context of GCM cloud physics (Bjordal et al., 2020; Bodas-Salcedo et al., 2019; Gettelman et al., 2019; Zhang et al., 2019). The uncertainty in ECS owing to SO SW_{FB} is still largely unconstrained by observations (Sherwood et al., 2020), with only a few studies explicitly focusing on evaluating SO SW_{FB} using the observational records of clouds, radiation, and meteorology (Terai et al., 2019, 2016; Ceppi, McCoy, & Hartmann, 2016; Gordon & Klein, 2014; Tan et al., 2019; Norris et al., 2016).

Many mechanisms have been proposed to explain the origins of negative SO SW_{FB} (Terai et al., 2019; Sherwood et al., 2020). One potential explanation is increasing liquid water content (LWC) from the warmer moist adiabat (Betts & Harshvardhan, 1987; Terai et al., 2019; Frazer & Ming, 2022). Shifts in the moist adiabat as the atmosphere warms will increase cloud LWC if the geometric height of clouds is preserved. As cloud temperature increases, the change in LWC per degree of warming decreases rapidly, so this mechanism is only salient in the high latitudes (Terai et al., 2019). Another potential mechanism is the increase in cloud LWC driven by shifts in the cloud phase (Senior & Mitchell, 1993; Tan et al., 2019, 2016; McCoy et al., 2014). As the atmospheric temperature rises, cloud condensates shifts from ice to liquid in the mixed-phased cloud regions. The total water content may also increase because liquid precipitates less efficiently than ice (Ceppi, Hartmann, & Webb, 2016; Frazer & Ming, 2022). In recent literature, a mechanism based on the connection between hydrological response and cloudiness change has been proposed to explain the increased LWC in extratropics (McCoy et al., 2022; McCoy, Field, Bodas-Salcedo, et al., 2020; McCoy et al., 2019). All aforementioned mechanisms may contribute to an increase in in-cloud LWC, which results in a negative cloud optical depth feedback (Stephens, 1978). Other mechanisms may contribute to changes in cloud coverage in the SO. These processes are restricted to boundary layer (BL) clouds. When the capping inversion at the top of BL increases with warming, the cloud top entrainment will be suppressed and lead to an increase in BL cloudiness (Bretherton et al., 2013; Myers & Norris, 2013; Qu et al., 2015). However, the cloud top entrainment may also increase with warming because of the increased vertical humidity gradient between BL and free troposphere (Bretherton et al., 2013; Frey & Kay, 2018; Rieck et al., 2012). This will reduce the BL cloudiness. The decoupling in the BL may increase with warming, preventing moisture transports from the surface into the cloud layer and also decreasing the low-cloud amount (Bretherton & Wyant, 1997; Bretherton et al., 2013; Zheng et al., 2020). All these hypothesized mechanisms may contribute to SO SW_{FB} and are entangled with each other, making process-level constraint of the SO SW_{FB} difficult (Terai et al., 2019; Frazer & Ming, 2022).

Here, we seek to provide a constraint on the GCM ensemble SO SW_{FB} using observed cloud properties and their covariability with meteorological state. The existing research has examined various cloud properties such as shortwave cloud radiative effect (SWCRE), albedo, cloud optical depth, and cloud fraction to provide observational constraints on the extratropical SW_{FB} (Gordon & Klein, 2014; Qu et al., 2015; Ceppi, McCoy, & Hartmann, 2016; Norris et al., 2016; Terai et al., 2016; Myers et al., 2021; McCoy et al., 2022). They generally support a positive SW_{FB} related to BL clouds and a negative SW_{FB} related to upper level clouds, and an overall negative extratropical SW_{FB}. Many of these studies have had to contend with the availability of GCM data and the challenges in characterizing SO clouds using visible radiation. GCM cloud fraction and cloud optical depth have to be processed with satellite simulators to enable direct comparison between model output and satellite retrievals (Bodas-Salcedo et al., 2011). The number of models that provide these outputs is very restricted, which limits evaluation of the shift in SO SW_{FB} spanning a large number of GCMs across CMIP5 and CMIP6 (Gordon & Klein, 2014; Ceppi, McCoy, & Hartmann, 2016). The SO also presents an observational challenge. Satellite retrievals of low-topped cloud properties like low-cloud fraction are difficult because of the multilayered structure of SO clouds (Qu et al., 2015; Haynes et al., 2011; Marchand et al., 2009; Sourdeval et al., 2016). Top-of-atmosphere (TOA) radiative flux derived quantities like SWCRE and albedo are more directly comparable to GCM output(Loeb et al., 2020), but they combine the effects of radiative processes as well as the response of clouds to meteorology. This makes it difficult to unpick how variations in TOA radiation are related to large-scale meteorology (Myers et al., 2021).

Area-mean column-integrated liquid water mass (LWP) is an advantageous cloud property for constraining SO cloud variability because the comparison between CMIP GCM output and low-frequency microwave radiometers is relatively straightforward. The LWP reported by GCMs and microwave observations is averaged over cloudy and cloud-free scenes and variability in LWP combines variability in cloud coverage and in-cloud LWC. LWP is a standard model output for all CMIP5/6 GCMs and can be directly compared to microwave observations without a satellite simulator as long as attention is paid to separating precipitating and non-precipitating liquid. Microwave LWP retrieval is not sensitive to multi-layered clouds, making it optimal for constraining SO cloud variability without partitioning by cloud top pressure regimes and accounting for overlap (McCoy et al., 2014). The response of area-mean LWP to warming is anti-correlated with SW_{FB} in the SO (Stephens, 1978; McCoy et al., 2022). For the above reasons, we choose to constrain the SO SW_{FB} across CMIP5 and CMIP6 models by constraining the response of LWP to warming.

We predict SO LWP response by the linkage between clouds and large-scale meteorology (so-called cloud-controlling factor (CCF) analysis, Stevens and Brenguier (2009)). Observations of clouds and their environment can be used to infer the response of clouds to long-term warming by assuming the relationships between clouds and large-scale meteorology are invariant from shorter observed periods (days - years) to climate change time-scale (years - century) (Klein et al., 2017). Surface temperature, stability, and large-scale subsidence have been widely used as environmental factors to predict cloud responses (Grise & Medeiros, 2016; Frey & Kay, 2018; McCoy, Field, Gordon, et al., 2020; McCoy, Field, Bodas-Salcedo, et al., 2020; Myers et al., 2021). In addition to these quantities, our CCF analysis considers large-scale moisture convergence. As shown in Held and Soden (2006), column-integrated water vapor increases with warming following Clausius-Clapeyron (C-C) scaling. Two direct consequences of increased humidity are increased horizontal transport of water vapor and enhanced existing patterns of moisture convergence and divergence. The latter change also satisfies the C-C scaling, albeit with spatial adjustments such as poleward expansion of the drying region (Siler et al., 2018; Bonan et al., 2023). Local precipitation and evaporation in the extratropics increase with warming but at a slower rate than C-C scaling owing to the energetic constraints (Allen & Ingram, 2002; Lorenz & DeWeaver, 2007; Stephens & Ellis, 2008; Trenberth, 2011; Yettella & Kay, 2017). The effects of a strengthening hydrological cycle in response to warming is consistent with how SO LWP responds to warming (McCoy et al., 2019). Because the conversion of water vapor to precipitation happens in clouds, increases in both the source and sink of clouds should guarantee an increase in cloudiness. In this work, we evaluate the linkage between the hydrological cycle and SO SW_{FB} by using moisture convergence as one of the large-scale meteorology factors to predict the SO LWP response (McCoy, Field, Bodas-Salcedo, et al., 2020; McCoy et al., 2022).

In addition to constraining the cloud response to meteorology, it is necessary to constrain the interactions between clouds and the radiation to constrain SW_{FB}. Previous work has shown that GCMs differ substantially in their simulation of how increasing cloudiness affects TOA upwelling SW flux (Bender et al., 2017). The intermodel differences in the radiative susceptibility of TOA SW flux to LWP contribute strongly to the intermodel difference in the SO SW_{FB} (McCoy et al., 2022). Model biases in simulating cloudiness changes in a perturbed climate are likely being compensated by the biases in the optical properties of simulated clouds. The so-called 'Too few, Too bright' bias has been diagnosed in previous generations of GCMs in the tropics (Nam et al., 2012; Konsta et al., 2022).

The goal of this paper it to use observations to constrain the SO SW_{FB} across 50 CMIP5 and CMIP6 GCMs (Table S1). A simplified physical model is developed to predict GCM SW_{FB} calculated from radiative kernels (Zelinka, Myers, McCoy, Po-Chedley, et al., 2020) by using the responses of LWP to warming combined with the susceptibility of radiation to liquid. Then, we constrain the LWP response to warming of GCMs by the observed covariability between LWP and large-scale meteorology, focusing on the role of hydrological response on SO SW_{FB}. Following this, we use satellite observations to calculate the susceptibility of radiation to liquid. Combining the constraints on LWP response and radiative susceptibility, we produce a constraint on the SO SW_{FB}. The paper is organized as follows. Section 2 describes the GCMs and observations, the simplified physical model, and how observations are used to constrain GCM SW_{FB}. In section 3, we conduct step-by-step constraints on the LWP response, radiative susceptibility, and the SO SW_{FB} of GCMs. Section 4 presents conclusions of this study and suggestions for future work on constraining extratropical SW_{FB}.

2 Data and Methodology

2.1 Data

We use 50 GCMs participating in CMIP5 (20) and CMIP6 (30) to provide the prior distribution of SO SW_{FB}. GCMs and their SO $(40-85^oS)$ SW_{FB} are listed in Table S1. The SW_{FB} for all GCMs are provided by Zelinka, Myers, McCoy, Po-Chedley, et al. (2020). For each GCM, Zelinka, Myers, McCoy, Po-Chedley, et al. (2020) calculate the response of SWCRE (clear-sky minus all-sky upwelling SW flux at TOA) to warming in the fully coupled 150-year CO_2 quadrupling ($abrupt4xCO_2$) simulation. SW_{FB} is obtained by adjusting the SWCRE response for non-cloud influences. This was completed by employing all- and clear-sky radiative kernels to discern the change in SWCRE due to clouds from other perturbations (e.g., water vapor, surface albedo, and external forcing) (Huang et al., 2017; Soden et al., 2008; Shell et al., 2008). The SW_{FB} output is spatially-resolved (1^o gridded) the region 90^oS - 90^oN.

We use monthly-mean LWP, global-mean near-surface temperature (GMT), large-scale meteorology, and TOA SW flux from fully-coupled preindustrial control (*piControl*) and $abrupt4xCO_2$ GCM simulations to construct a simplified physical model linking variabilty in LWP to SW_{FB}. Using monthly-mean output instead of higher temporal resolution output allowed us to survey nearly all CMIP5 and CMIP6 GCMs. LWP is the column-integrated liquid water mass averaged over cloudy and cloud-free portions of the model gridbox, which can be related to in-cloud LWP and cloud fraction since LWP $\approx$ cloud fraction $\times$ in-cloud LWP. LWP is computed as the difference between CMIP variables *clwvi* (total condensed water path) and *clivi* (ice water path, IWP). We calculate the change in GMT (*tas*) in each GCM to normalize the change in LWP for consistency with the calculation of SW_{FB} (Zelinka, Myers, McCoy, Po-Chedley, et al., 2020). Four descriptors of large-scale meteorology are used to predict the SO LWP: surface skin temperature (T_s; labeled *ts* in CMIP output); precipitation minus evaporation ($P-E$; *pr* and *hfls*), a proxy for moisture convergence ; lower-tropospheric stability (LTS; calculated from *ta* at 700 mb, *ps*, and *ts*) (Klein & Hartmann, 1993), and subsidence at 500 mb (ω_{500}; *wap*). Note that T_s refers to the skin temperature of Earth's surface, which differs from the near-surface air temperature used to calculate GMT (output from CMIP as *tas*). For the open ocean, T_s is the sea surface temperature. GCM radiative susceptibility is calculated from the TOA albedo (α calculated from the CMIP outputs $rsut/rsdt$), LWP, and clear-sky albedo ($\alpha_{cs} = rsutcs/rsdt$) (section 2.2.4). Anomalies (between abrupt CO2 quadrupling and pre-industrial control) are computed as the difference between the mean of years 121-140 of $abrupt4xCO_2$ and the average of $piControl$ simulations following Bjordal et al. (2020); Myers et al. (2021).

Satellite observations and reanalysis are used to constrain the LWP covariance with meteorology and the radiative covariance with LWP. Monthly-mean LWP is provided by the Multisensor Advanced Climatology of Liquid Water Path (MAC-LWP) (Elsaesser et al., 2017b). MAC synthesizes passive microwave observations of cloud LWP from multiple satellites. It provides 1^o gridded total LWP output averaged over cloudy and cloud-free scenes, which makes it directly comparable to GCM LWP. However, microwave retrievals are only available over open water, which limits our ability to constrain the LWP response over sea ice.

Monthly-mean GMT and large-scale meteorology are described by Modern-Era Retrospective analysis for Research and Applications, Version 2 (MERRA-2) reanalysis (Gelaro, McCarty, Suárez, et al., 2017). LWP, GMT, and large-scale meteorology observations from 1992 to 2016 are used to test whether the chosen large-scale meteorology can predict observed LWP (section 3.1.1). The observed covariance between LWP and meteorology is used to constrain the GCM LWP response (section 3.1.2). Monthly-mean TOA SW fluxes are provided by the Clouds and the Earth's Radiant Energy System (CERES) Energy Balanced and Filled (EBAF) Edition 4.1 product (Loeb et al., 2018b). The observed clear-sky flux in Edition 4.1 is adjusted to be consistent with the definition of GCM clear-sky flux (Loeb et al., 2020). The TOA SW fluxes and LWP from 2003 to 2016 are used to constrain the GCM radiative susceptibility (section 3.2) based on the availability of CERES and MAC-LWP data.

2.2 Methods

2.2.1 Simplified Physical Model for Predicting SW Cloud Feedback

In this work we seek to understand drivers of SW_{FB}. To this end, we develop a simplified physical model to predict the SO SW_{FB}. To give context to and motivate this analysis we provide a brief survey of the cloud and radiation response to warming in CMIP5 and CMIP6 GCMs. Figure 1a shows the SW_{FB} and LWP responses to increases in GMT for the GCMs surveyed in this study (written as $\Delta LWP/\Delta GMT$). Across GCMs, the LWP response is anti-correlated with model SW_{FB} and reproduces the dipole pattern of feedback in the SO (Figure 1b). GCMs with a larger increase in LWP in response to rising GMT tend to have more strongly negative SW_{FB}. While LWP generally increases with GMT, there are a few GCMs reporting decreasing LWP after the first few degrees of warming (Figure 1b). One goal of this study is to understand why these models behave differently from the majority of GCMs where LWP increases in step with GMT (section 3.1.3). This correspondence between LWP response to warming and SW_{FB} in the SO suggests that LWP can be used to describe how cloud macrophysical state drives cloud feedback in this region, consistent with previous studies (McCoy et al., 2022).

A simplified, but physical, model can be built to predict SW_{FB} based on the linkage between the change in liquid cloudiness and its effect on TOA radiative flux. SW_{FB} is the change in upwelling SW flux at TOA ($\Delta SW_{\uparrow}$) due to the adjustment of cloud properties, normalized by the change in GMT ($\Delta SW_{\uparrow C}/\Delta GMT$) (Zelinka, Myers, McCoy, Po-Chedley, et al., 2020). Because the downwelling SW flux at TOA ($SW_{\downarrow}$) is only a function of months and latitudes, local SW_{FB} at a given month is proportional to the cloud-induced change in TOA albedo ($\alpha = SW_{\uparrow}/SW_{\downarrow}$) and normalized by GMT ($\Delta\alpha_C/\Delta GMT$). In turn, the response of α to warming can be approximated as the product of the susceptibility of α to liquid ($\partial\alpha/\partial LWP$) and the response of cloud liquid to warming ($\Delta LWP/\Delta GMT$), as follows

$$SW_{FB} = -\frac{\Delta SW_{\uparrow C}}{\Delta GMT} \propto -\frac{\Delta\alpha_C}{\Delta GMT} \sim -\frac{\partial\alpha}{\partial LWP} \cdot \frac{\Delta LWP}{\Delta GMT} \tag{1}$$

This model derives from previous work (McCoy et al., 2022). Equation 1 is used to predict GCM SW_{FB} calculated from radiative kernels (Zelinka, Myers, McCoy, Po-Chedley, et al., 2020). Equation 1 makes several simplifications based on the limitations of GCMs and observational data. Two simplifications central to the formulation of equation 1 are detailed below.

First, SW_{FB} is proportional to $\Delta\alpha_C/\Delta GMT$ for a given latitude and time. As mentioned in section 2.1, LWP observations are only available over open water, so we can not provide apples-to-apples observational constraints on the $\Delta LWP/\Delta GMT$ and $\partial\alpha/\partial LWP$ for high latitudes. We average $\Delta LWP/\Delta GMT$ and $\partial\alpha/\partial LWP$ to allow regional constraints.

Second, we neglect changes in albedo ($\Delta\alpha_C$) driven by changes in ice cloud in response to warming. We make this approximation for two reasons. First, there is no equivalent observational data set to MAC-LWP for IWP, making it difficult to offer an effective observational constraint on the response of IWP to global warming. Second, IWP response (ΔIWP) to warming contributes minimally to a GCM SW_{FB} in this region (McCoy et al., 2022). This is due to a combination of the smaller magnitude of $\Delta IWP/\Delta GMT$ compared to $\Delta LWP/\Delta GMT$ in the SO (McCoy et al., 2016) and the weaker scattering of SW radiation per unit mass of ice compared to liquid due to the smaller size of typical liquid droplets relative to ice crystals (Liou, 2002; McCoy et al., 2014). Section 3.3 evaluates the effect of neglecting ice on the results of this study.

As with any approximate model, the predictive ability of our model is degraded by the simplifications. The model in Equation 1 is balance between simplicity and accuracy. Uncertainty introduced by the simplifications will be reflected in the statistical uncertainty in the equation 1 prediction of GCM-derived SW_{FB}. This is similar to other studies seeking to develop a simplified, but interpretable, model that can explain variability in the Earth system (Held & Soden, 2006; Qu et al., 2015). We constrain the SO SW_{FB} by providing constraints on the GCM LWP response ($\Delta LWP/\Delta GMT$) and the radiative susceptibility ($\partial\alpha/\partial LWP$) separately. Constraint methods are discussed in the following sections.

2.2.2 Prediction of LWP using Cloud-Controlling Factor Analysis

In this section we examine the linkage between LWP and large-scale meteorology. The large-scale environmental factors affecting local cloud properties are referred to as cloud-controlling factors (Stevens & Brenguier, 2009). CCF analysis is based on the idea that the response of cloud properties to global warming can be expressed by a first-order Taylor expansion in CCFs (Klein et al., 2017). One application of this framework in the literature is to use observations to constrain LWP response to GCM-predicted changes in CCFs (Qu et al., 2015; Klein et al., 2017). Following Qu et al. (2015), we predict the response of LWP to GMT as

$$\frac{\Delta LWP}{\Delta GMT} = \sum_i \frac{\partial LWP}{\partial X_i} \frac{\Delta X_i}{\Delta GMT} + Res \tag{2}$$

where X_i are CCFs. Equation 2 decomposes LWP response to GMT into the LWP responses to CCFs and a residual term. LWP response to GMT induced by each CCF is a product of the sensitivity of LWP to each CCF ($\partial LWP/\partial X_i$) and the response of that CCF to GMT ($\Delta X_i/\Delta GMT$). The CCF model shown in equation 2 is trained on $piControl$ simulations of each GCM to calculate $\partial LWP/\partial X_i$. The $\Delta X_i/\Delta GMT$ term is given by the differences between $piControl$ and $abrupt4xCO_2$ simulations of each GCM. Compared to clouds, CCFs suffer from less parametric uncertainty in GCMs because they are aspects of the resolved large-scale processes (Qu et al., 2015; Klein et al., 2017). Using equation 2, we can provide a constraint on the LWP response to GMT by replacing the $\partial LWP/\partial X$ derived from $piControl$ simulations of GCMs with the values derived from observations and using GCM estimates of $\Delta X_i/\Delta GMT$. As discussed in the introduction, an important assumption underlying CCF analysis is that the relationships between clouds and CCFs are time-scale invariant (Qu et al., 2015; Klein et al., 2017). We test this assumption in section 3.1.

The CCFs (X_i) considered in this study are surface skin temperature (T_s), precipitation minus evaporation ($P{-}E$), lower tropospheric stability (LTS) (Klein & Hartmann, 1993; Slingo, 1980), and 500 mb subsidence (ω_{500}). These CCFs are consistent with previous studies of covariance between extratropical clouds and meteorology (McCoy, Field, Bodas-Salcedo, et al., 2020; McCoy et al., 2022; Zelinka, Myers, McCoy, Po-Chedley, et al., 2020; Zelinka et al., 2018).

We use $P{-}E$ as a proxy for moisture convergence because moisture convergence is not output from GCMs participating in CMIP5 and CMIP6. These two terms differ by the change in moisture storage over time (Seager & Henderson, 2013). To demonstrate that these quantities are nearly identical for our study, we examine the fifth generation European Centre for Medium-Range Weather Forecasts (ECMWF; ERA5) for both variables, $P - E$ is a close approximation of moisture convergence in $40 - 85^oS$ when we averaged them in 5^o x 5^o gridbox of monthly output (Figure S1 in the supplementary information). The discrepancy between these two variables in GCMs should be smaller than in reanalysis because of the absence of an analysis increment in GCMs (Seager & Henderson, 2013). For these reasons, we will average GCM LWPs and CCFs as well as observations over 5^o x 5^o gridboxes within $40{-}85^oS$ to conduct the CCF analysis. The LWP response is predicted by the CCF model (Equation 2) in each 5^o x 5^o gridbox in the SO.

$P{-}E$ is consistently positive in $40{-}85^oS$ across all GCMs in the mean state climate ($piControl$ simulation) (gray lines in Figure S2). In $abrupt4xCO_2$ simulations, $P-E$ reduces in the $40 - 50^oS$ region and enhances across the $50 - 85^oS$ region (colored lines in Figure S2). This is consistent with a poleward expansion of subtropical drying region under global warming (Siler et al., 2018; Bonan et al., 2023) and a robust moistening of latitudes poleward of 50^oS (Held & Soden, 2006). Comparing moisture convergence response to warming and SW_{FB} suggests that 50^oS may act as a demarcation between positive SW_{FB} (negative $\Delta LWP/\Delta GMT$) and negative SW_{FB} (positive $\Delta LWP/\Delta GMT$) estimated from $abrupt4xCO_2$ simulations of CMIP5 and CMIP6 GCMs (Figure 1a) due to changes in moisture convergence regime. This is consistent with the notion that the hydrological response to warming (Held & Soden, 2006) sets some of the pattern of SW cloud feedback in the SO (McCoy et al., 2022). To characterize this feature, we present our analysis separately for the $40{-}50^oS$ and $50{-}85^oS$ regions (sections 3.1.2 and 3.3).

We use monthly-mean data to examine the covariance between LWP and $P - E$. This enables averaging across the synoptic systems that drive extratropical moisture convergence (Field & Wood, 2007). This approach is not particularly new and many previous studies have leveraged monthly mean CCFs to predict extratropical cloudiness (Zelinka, Myers, McCoy, Po-Chedley, et al., 2020; Zelinka et al., 2018; Ceppi, McCoy, & Hartmann, 2016). We believe this averaging doesn't substantially degrade our results based on previous studies relating LWP in extratropical cyclones to moisture convergence (McCoy et al., 2019; McCoy, Field, Bodas-Salcedo, et al., 2020). We don't expect that monthly averages will strongly degrade the predictive capacity of our CCF model since previous studies examining daily means suggest fairly linear dependence of LWP on CCFs (McCoy et al., 2018; McCoy, Field, Bodas-Salcedo, et al., 2020). We test whether performing our analysis on monthly means degrades the predictive ability of our model using two out-of-sample tests.

2.2.3 Cloud Regime Temperature-dependence

CCF analysis has been used in numerous studies to predict the response of clouds to warming in the tropics and subtropics (Qu et al., 2015; Zhai et al., 2015; Myers & Norris, 2016; Brient & Schneider, 2016; McCoy et al., 2017; Myers et al., 2021; Wall et al., 2022) as well as the extratropics (Ceppi, McCoy, & Hartmann, 2016; Zelinka, Myers, McCoy, Po-Chedley, et al., 2020; Zelinka et al., 2018). The SO region present a challenge to a CCF model that lumps together all clouds into a single set of sensitivities between clouds and CCFs (i.e, equation 2). From $40 - 85^oS$, T_s varies from 210 K in the austral winter over the Antarctic continent to around 290 K in the summer subtropics. The temperature of the atmosphere and clouds varies along with T_s. The wide range of cloud temperatures results in a combination of mixed-phase clouds and liquid-only clouds in the SO (Tan et al., 2016).

The formation and removal processes governing liquid and mixed-phase clouds are very different (Morrison et al., 2012). Precipitation efficiency is higher in mixed-phase clouds than in liquid-only clouds due to the rapid growth of ice crystals at the expense of liquid drops (Storelvmo & Tan, 2015). The higher precipitation efficiency of mixed-phase clouds results in the majority of mid-latitude precipitation events originating as snow (Field & Heymsfield, 2015). Previous studies suggest that mixed-phase and liquid-only clouds will respond differently to global warming (Tan et al., 2016). GCM low cloud optical depth increases with warming for cold clouds and decreases with warming for warm clouds (Gordon & Klein, 2014; Terai et al., 2016). This behavior is also found in in-situ observations (Terai et al., 2019).

Because of the differing cloud physics and potential cloud feedback processes arising due to cold (mixed-phase) and warm (liquid-only) clouds, we split our CCF model over temperature. The intent of splitting our CCF model over temperature is to separate the SO into regions that are only mixed-phase and only liquid-only clouds, which is not really possible in the context of climate model output at monthly resolution, but to separate the SO into regimes that are dominated by different processes and therefore LWP covaries with CCFs differently. We count a 5^o x 5^o gridbox in $40{-}85^oS$ as a cold (warm) regime gridbox if the mean T_s of gridbox is lower than (larger or equal to) a threshold T_s (TR_{T_s}). This results in a CCF model split over TR_{T_s}:

$$
\begin{aligned}
\frac{\Delta LWP}{\Delta GMT}|_{Cold} &= \sum_i (\frac{\partial LWP}{\partial X_i}|_{Cold} \cdot \frac{\Delta X_i}{\Delta GMT}|_{Cold}) + Res_1 \\
T_s &< TR_{T_s} \\
\frac{\Delta LWP}{\Delta GMT}|_{Warm} &= \sum_i (\frac{\partial LWP}{\partial X_i}|_{Warm} \cdot \frac{\Delta X_i}{\Delta GMT}|_{Warm}) + Res_2 \\
T_s &\geq TR_{T_s}
\end{aligned}
\tag{3}
$$

We have two goals in our methodology for determining TR_{T_s} for each GCM. First, we want to make the determination of TR_{T_s} objective for each GCM. Second, we want to make the determination of TR_{T_s} in a way that allows an analogous calculation for observations. For each GCM, TR_{T_s} is defined as the threshold T_s that maximizes the explained variance in mean-state (*piControl*) LWP by the CCF model in equation 3. For each GCM we iterate through possible TR_{T_s} values within the entire range of T_s within the SO latitudes and calculate the coefficient of determination (R^2) of equation 3 when predicting *piControl* LWP (Figure S3 in the supplementary information). Equation 3 explains more than 70 % of the variance of *piControl* LWP across GCMs. One question is whether TR_{T_s} is time scale invariant. In Figure S4 of the supplementary information, we calculate TR_{T_s} using $abrupt4xCO_2$ data instead of *piControl* . The TR_{T_s} trained using $abrupt4xCO_2$ simulations correlates with TR_{T_s} trained from *piControl* simulations, supporting that TR_{T_s} is time-scale invariant. We use the TR_{T_s} trained on *piControl* simulations to predict the LWP response to warming in $abrupt4xCO_2$ simulations (section 3.1.2). The TR_{T_s} for most GCMs is around 270 K (Figure S3), which generally separates the clouds over cold ice or land surfaces from the open ocean. Komurcu et al. (2014) shows that the supercooled liquid fraction in GCMs dramatically drops when cloud temperature is lower than 255 K. Assuming a typical extratropical environment with cloud base height of $2-3$ km and lapse rate of 6.5 K/km, its T_s would be close to 270 K. This is consistent with the idea that mixed-phased and liquid-only clouds have different cloud physics and response behaviors to their environments.

Because microwave radiometers do not retrieve LWP over ice (Elsaesser et al., 2017b), we need to consider sampling differences between GCMs and observations when providing observational constraints. The region for which valid data is available from MAC is very similar to GCM warm regimes (Figure S5). In the remainder of this study observational constraint is only available for the warm regime of equation 3 and all the cold regime observations are treated missing due to lack of observations.

2.2.4 Radiative Susceptibility

In equation 1, the response of LWP to GMT is connected to its SW radiative effect through a radiative susceptibility term ($\partial\alpha/\partial LWP$). This term describes how a change in LWP affects α while keeping other factors fixed. Following McCoy et al. (2022), the radiative susceptibility is estimated by training the multi-linear regression model

$$\alpha = c_1 * LWP + c_2 * \alpha_{clear-sky} + c_3 \tag{4}$$

where c_1 is $\partial\alpha/\partial LWP$. The regression model is trained on *piControl* GCM simulations and observations to obtain radiative susceptibilities for GCMs and observations. Training is performed at the native spatial resolution of the data. TOA albedo α is a function of clear-sky albedo (α_{cs}) and LWP, while LWP is in turn affected by cloud areal extent (Bender et al., 2017) and cloud optical depth (Gordon & Klein, 2014). By including α_{cs} as a predictor we seek to separate the change in α contributed by changes in clouds from non-cloud perturbations (e.g., surface conditions). This is consistent with calculating SW_{FB} by adjusting the SWCRE response for non-cloud influences using radiative kernels (Zelinka, Myers, McCoy, Po-Chedley, et al., 2020; Soden et al., 2008).

One way to think of equation 4 is a very simple radiative kernel. To enable the use of equation 4 we subset our training data to remove cases where surface albedo or near surface sun angle strongly affect TOA albedo. The sensitivity of TOA upwelling SW flux to changes in cloudiness over a bright surface is low because of the high surface albedo. Consequently SW_{FB} is nearly zero over surface ice (i.e. the Antarctic continent) (Shell et al., 2008). We train equation 4 over open water to minimize the effect of extremely bright surfaces on the calculation of $\partial\alpha/\partial LWP$. We subset training data using a clear-sky albedo threshold ($TR_{\alpha_{cs}}$). We evaluate the sensitivity of $\partial\alpha/\partial LWP$ to the value of $TR_{\alpha_{cs}}$ in section 3.2. Increasing solar zenith angle increases albedo (McCoy et al., 2018). Compounding this effect, LWP decreases in winter while solar zenith angle increases. Data from a single month is used to calculate the radiative susceptibility $\partial\alpha/\partial LWP$ to reduce the effects of spurious covariation between solar zenith angle and LWP. We choose January because austral summer is the time that the change in LWP contributes the most to SW_{FB} when insolation is strong.

3 Results

3.1 Predicting LWP

The first step to providing an observational constraint on SW_{FB} using equation 1 is to constrain the response of SO LWP to warming using observed covariability between CCFs and LWP. To understand the uncertainty in our CCF-based constraint of LWP response we need to evaluate whether the relationships between LWP and CCFs are invariant across time scales (Klein et al., 2017). Two out-of-sample tests are performed to test time scale invariance, and more broadly, to test the predictive skill of the CCF model. First, we train a CCF model (equation 2) on monthly-mean observations for a short period and use it to predict the interannual variability of LWP back to 1992. This is shown in section 3.1.1. Second, we train the regression model in equation 3 on monthly-mean *piControl* simulations and use it to predict the GCM-simulated response of LWP to CO_2 quadrupling. This is discussed in section 3.1.2. Following these tests, we use the LWP-CCF relationships obtained from observations to constrain the LWP responses in GCMs in section 3.1.2. In section 3.1.3, we discuss GCM LWP responses by apportioning $\Delta LWP/\Delta GMT$ among the CCFs.

3.1.1 Predicting Historical Trends in LWP

Observations of LWP are available from 1992-2016. We this period into a training period (2012-2016) and a validation period (1992-2011). Equation 2 is trained on 2012-2016 to calculate $\partial LWP/\partial X_i$. Equation 2 is used to predict the interannual variation of LWP 1992-2011. MAC-LWP observes an increase in SO LWP over the past two decades, consistent with Manaster et al. (2017) and Norris et al. (2016) (Figure 2a). The predicted LWP from equation 2 broadly reproduces the positive trend of LWP during the period from 1996 onward (Figure 2a). Before 1996, the LWP trend predicted by the CCF model is negative. This may be because the CCFs predicted by MERRA-2 are reliant on the observations being ingested into the reanalysis. Many fewer observations of precipitation are available before the mid-1990s (Gelaro, McCarty, Suárez, et al., 2017). The lack of observational input to reanalysis may lead to the disagreement between the LWP predicted by the CCF model and LWP observations in the early 1990s. During the period where numerous observations were available to the MERRA-2 reanalysis, the ability of CCF model in equation 2 to reproduce the decadal-scale trend and interannual variability of LWP in an out-of-sample test supports the time-scale invariance of $\partial LWP/\partial X_i$. The ability of the CCF model to reproduce the observed trend in LWP is not sensitive to the choice of training and validation periods (Figure S6).

Equation 2 can be used to decompose the predicted trend into contributions from individual CCFs. The positive decadal trend in SO LWP can be largely explained by the increase in $P-E$ (Figure 2b). Increases in T_s explain only a small fraction of the LWP trend. Stability and large-scale subsidence have negligible effects on the SO LWP on a decadal scale. Increased $P-E$ is related to the increased moisture content in the extratropical atmosphere (Held & Soden, 2006). This result suggests that the hydrological cycle has played an important role in the response of SO LWP to increased GMT over the past two decades (Norris et al., 2016; Manaster et al., 2017).

3.1.2 Predicting LWP response to CO_2 Quadrupling

Following our evaluation of time-scale invariance of $\partial LWP/\partial X_i$ in observations, we evaluate whether the $\partial LWP/\partial X_i$ trained using *piControl* GCM data can be used to predict the LWP response in $abrupt4xCO_2$ simulations. Figure 3 shows the changes in LWP in response to warming ($\Delta LWP/\Delta GMT$) between the average of *piControl* and the mean of years 121-140 of $abrupt4xCO_2$ simulations (Myers et al., 2021; Bjordal et al., 2020). Predicted LWP responses are shown in three latitude bands: $40-85^oS$ (Figure 3 left); $40-50^oS$ (Figure 3 middle); and $50-85^oS$ (Figure 3 right). The CCF model (equation 3) predicts 70% of GCM variance in $\Delta LWP/\Delta GMT$ in the latitude band encompassing the SO (Figure 3b). This supports the time-scale invariance of $\partial LWP/\partial X_i$. The explained variance in the $40-50^oS$ latitude band is 60% (Figure 3d). This decrease in explained variance relative to the entire SO may be related to the hydrological response in this region. While moisture is converged into $40-50^oS$ in the mean-state climate, the convergence pattern becomes less robust at the end of $abrupt4xCO_2$ simulations. Some GCMs display drying and some display moistening in $40-50^oS$ (Figure S2). In the latitude band where warming simulations consistently predict moistening ($50-85^oS$), the explained variance in $\Delta LWP/\Delta GMT$ is 86% (Figure 3f).

Because observational constraint from MAC-LWP is only available in the warm regime, we separate the predictions of CCF model into warm and cold regimes for each latitude band. The LWP response to GMT in the warm regime predicts the majority of total LWP response across latitude bands (Figure 3ace). Only the warm regime exists in the $40-50^oS$ region, so $r^2 = 1$ (Figure 3c). The explained variance in $\Delta LWP/\Delta GMT$ by warm regime is still high in the $50-85^oS$ region ($r^2 = 0.64$, Figure 3e).

We calculate how observations in the warm regime in each latitude band constrain overall $\Delta LWP/\Delta GMT$. The $\partial LWP/\partial X_i$ for each GCM in the warm regime is replaced with the $\partial LWP/\partial X_i$ computed from observations yielding a constraint on $\Delta LWP/\Delta GMT$ in the warm regime. This constraint is propagated from the warm regime to the aggregate of both regimes. Uncertainty in the best fit line fit relating the CCF prediction of the warm regime to the CCF prediction of both regimes is estimated by Jackknife resampling (Tukey, 1958). We intersect the shaded regions on the x-axis in Figure 3ace with the best-fit lines and their uncertainties to propagate the warm regime constraint to both regimes for each latitude band. The observational constraint on $\Delta LWP/\Delta GMT$ for each latitude band is then propagated through the uncertainty from the CCF model. In Figure 3bdf, the constrained ranges from the y-axis of Figure 3ace are denoted via intersection of the brown shading with the x-axis. The best fit lines and uncertainty in Figure 3bdf are used to propagate the constraints on the CCF model predictions to the GCM simulated LWP response. These constraints are used in section 3.3 to constrain SW_{FB}. Once propagated, observational constraints on the warm regime point towards a moderate $\Delta LWP/\Delta GMT$ across the SO.

Potential systematic biases in the passive microwave observations of LWP can be propagated to uncertainty in our constraint on $\Delta LWP/\Delta GMT$. Observational biases in LWP impact constraints on $\Delta LWP/\Delta GMT$ by affecting the observed sensitivities of LWP to CCFs ($\partial LWP/\partial X$). Potential systematic biases in microwave LWP observations are estimated following Greenwald et al. (2018). The net bias of LWP in the SO (poleward to 40^oS) should be smaller than $+10\ g/m^2$ and is relatively spatially uniform

(Figure 17(f) and Figure 19(a) in Greenwald et al. (2018)). The LWP percentage bias is ± 10.8%, calculated by dividing ±10 g/m^2 by the averaged LWP during the observational training period. We then recalculate $\partial LWP/\partial X_i$ by perturbing the observational values of LWP by ±10.8%. Considering potential observational LWP bias slightly loosens the constraint of $40-85^oS$ $\Delta LWP/\Delta GMT$ from [2.76, 4.19] $g\ m^2\ K^{-1}$ to [2.60, 4.47] $g\ m^2\ K^{-1}$. The effect of observational bias is propagated through to the constraint on the SO SW_{FB} in section 3.3.

3.1.3 CCF Contributions to LWP Response to CO_2 Quadrupling

In this section we show the sensitivities of LWP to CCFs ($\partial LWP/\partial X_i$) as well as each CCF's contribution to the LWP response to warming following similar analysis in previous studies (Zelinka, Myers, McCoy, Po-Chedley, et al., 2020). $\partial LWP/\partial X_i$ for each GCM (Figure 4a) can be scaled by the change in each CCF between $piControl$ and the end of $abrupt4xCO_2$ simulation ($\Delta X_i/\Delta GMT$; Figure 4b) to yield the contribution of each CCF to $\Delta LWP/\Delta GMT$ (Figure 4c; equation 3). Cold and warm regime predictions are shown separately. Observed $\partial LWP/\partial X$ are only available for the warm regime (Figure 4a).

The dependence of LWP on CCFs across GCMs and observations (Figure 4a) is broadly consistent with previous studies. The coefficient relating LWP and T_s ($\partial LWP/\partial T_s$)is positive across all GCMs for the cold regime. Agreement between GCMs on the sign of $\partial LWP/\partial T_s$ decreases for the warm regime. This is consistent with previous studies suggesting that cold cloud optical depth increases in response to warming (Gordon & Klein, 2014; Terai et al., 2019), mostly due to the increased cloud water content (Betts & Harshvardhan, 1987). Terai et al. (2019) suggests that the cloud optical depth for warm clouds may decrease or stay constant with increasing temperature owing to the reduced cloud adiabaticity. The coefficient relating LWP to $P-E$ ($\partial LWP/\partial P-E$) is positive for warm and cold regimes, which is consistent with previous literature (McCoy et al., 2019; McCoy, Field, Bodas-Salcedo, et al., 2020). The coefficient relating LWP and LTS ($\partial LWP/\partial LTS$) is mostly positive in the warm regime of GCMs, while the coefficient relating LWP to ω_{500} ($\partial LWP/\partial\omega_{500}$) is small. This is consistent with previous work on boundary layer cloudiness (Zelinka et al., 2018; Myers & Norris, 2015, 2013). Observed $\partial LWP/\partial T_s$ and $\partial LWP/\partial P-E$ are positive and much larger than $\partial LWP/\partial LTS$ and $\partial LWP/\partial\omega_{500}$.

Both T_s and $P-E$ increase with warming in warm and cold regimes (Figure 4b). LTS increases with warming in the warm regime but decreases in the cold regime. This pattern may be related to the poleward shift of the Hadley cell (stabilizing the warm regime lower troposphere) and the poleward shift of the Southern Hemisphere storm track (destabilizing the cold regime lower troposphere) simulated by GCMs (Barnes & Polvani, 2013; Bender et al., 2012). The variation in large-scale subsidence is relatively small compared to other CCFs.

Combining $\partial LWP/\partial X_i$ and the response of CCF to warming ($\Delta X_i/\Delta GMT$) allows us to apportion $\Delta LWP/\Delta GMT$ among CCFs. In the warm regime, GCMs have roughly equivalent contributions due to T_s, $P-E$, and LTS. In the cold regime, $P-E$ and T_s changes contribute the most (Figure 4c).

Among the GCMs surveyed here (Table S1), the second Community Earth System Model (CESM2), its variants (CESM2-WACCM, CESM2-FV2, CESM2-WACCM-FV2), and E3SM-1-0 predict a decrease in LWP after the first few degrees of warming in $abrupt4xCO_2$ simulations (Figure 1b), which is consistent with previous studies (Bjordal et al., 2020). These models share a similar atmosphere component (Danabasoglu et al., 2020; Golaz et al., 2019; Rasch et al., 2019). Focusing on CESM2 in Figure 4, characterizes how decreases in LWP as GMT increases relate to CCFs. The prediction of CESM2's LWP response to warming by equation 3 trained on $piControl$ is less skillful than the prediction for other GCMs (Figure S7), but it is improved relative to previous CCF-based predictions (McCoy et al., 2022). While work is required to more accurately predict the CESM2 LWP response using a CCF model, the decreased LWP in the warm regime is captured by equation 3 (Figure 4c and Figure S7). Decomposing the prediction from equation 3 suggests that the LTS-induced increase in CESM2 LWP in the warm regime is offset by decreases related to T_s. CESM2 displays the lowest warm regime $\partial LWP/\partial P - E$ and the $P{-}E$ contribution to LWP response is small (Figure 4ac). Relative to observations CESM2 overestimates $\partial LWP/\partial LTS$ and underestimates $\partial LWP/\partial P - E$ in the warm regime. Warm regime $\partial LWP/\partial T_s$ is negative in CESM2, but is positive in observations (Figure 4a). Warm regime T_s, $P - E$, and LTS increase in response to GMT (Figure 4b) and the net effect is a negative trend in LWP beyond the first degree of warming with an the overall near-zero response of LWP to warming.

As mentioned in the introduction, the phase shift in mixed-phased clouds is one of the potential mechanisms that may contribute to the increase in SO LWP that in turn drives a negative SW_{FB} (Tan et al., 2016). Bjordal et al. (2020) attribute the high climate sensitivity of CESM2 to its large mean-state supercooled liquid fraction (i.e., small ice fraction) in the SO because its low-level clouds are easily shifted to being liquid-dominated and the contribution of the negative cloud phase feedback reduces as GMT increases. We examine this idea in the context of our analysis framework by examining the state dependence of $\partial LWP/\partial T_s$. In the context of our CCF model, $\partial LWP/\partial T_s$ may indicate the contribution to LWP change by shifts between ice and liquid. As with any other correlative analysis caution should be used in interpreting this metric since it may also related to other processes such as shifts in the moist adiabat.

Following Bjordal et al. (2020), we calculate $\partial LWP/\partial T_s$ in 15-year chunks during the 150 years of $abrupt4xCO_2$ simulations to contrast how this sensitivity evolves with warming across GCMs (Text S1). We find that CESM2 is an outlier among the GCMs surveyed here in regards to how $\partial LWP/\partial T_s$ changes with time (Figure S8 in the supplementary information). $\partial LWP/\partial T_s$ shifts toward more negative values as warming continues. This behavior is not displayed in other GCMs. This is consistent with the analysis of CESM2 in Bjordal et al. (2020). For GCMs like CESM2 that have large supercooled liquid fractions, as the climate warms the ice available for transition to liquid is decreased and the phase shift-related changes in LWP are reduced. This may explain the non-monotonic response of LWP to warming that is displayed in CESM2.

3.2 Radiative Susceptibility

Following equation 1, we argue that SW_{FB} can be approximated as proportional to the product of change in LWP and the sensitivity of albedo to LWP. Across GCMs, $\partial\alpha/\partial LWP$ vary by nearly a factor of seven. One emergent behavior in GCMs is an inverse relationship between $\partial\alpha/\partial LWP$ and mean-state LWP. This is consistent with previous studies (McCoy et al., 2022). TOA albedo and cloud fraction (areal coverage of clouds) are approximately linearly related until the scene becomes overcast (Bender et al., 2017). The effect of in-cloud LWP on albedo saturates at high in-cloud LWP (Lacis & Hansen, 1974). The SO mean-state LWP is a function of cloud fraction and in-cloud LWP. A GCM that simulates high mean-state LWP has fewer clear-sky pixels that can be filled and is closer to radiative saturation. As LWP increases with warming, additional liquid affects α less efficiently by only increasing the in-cloud liquid rather than increasing cloud coverage.

Radiative susceptibility calculated from CERES and MAC-LWP observations is low relative to GCMs (Figure 5). This result suggests that the too-bright and too-homogeneous bias of tropical clouds in CMIP6 GCMs (Konsta et al., 2022) may also exist in the simulation of extratropical clouds. One potential uncertainty in estimating $\partial\alpha/\partial LWP$ is the clear-sky albedo threshold ($TR_{\alpha_{cs}}$) applied before training the regression model in equation 4. We include this uncertainty in the SW_{FB} constraint by calculating $\partial\alpha/\partial LWP$

varying $TR_{\alpha_{cs}}$ from 0.11 to 0.30 (0.105 is lowest clear-sky albedo for some GCMs). This uncertainty range is compounded by potential systematic uncertainty in observed LWP as discussed above. When both sources of uncertainty are included, the range of observed susceptibility widens from $[0.43, 0.90]$ $(kg\ m^{-2})^{-1}$ to $[0.39, 1.01]$ $(kg\ m^{-2})^{-1}$.

One intriguing feature of GCMs is that GCMs where SO LWP is more sensitive to the hydrological cycle (large $\partial LWP/\partial P - E$) tend to have a weaker radiative response (small $\partial\alpha/\partial LWP$). This results in a buffering between macrophysical cloud response to GMT and radiative response to GMT. We examine how radiative and macrophysical factors are linked through mean-state LWP. $\partial LWP/\partial P - E$ positively correlates with mean-state LWP in both cold and warm regimes (Figure 5). This relationship can be explained in the context of sources and sinks of cloud liquid content (McCoy, Field, Bodas-Salcedo, et al., 2020; McCoy et al., 2022). Source and sink rates of clouds can be written as

$$\begin{aligned} K_{source} &= e_{source} \cdot r_{water\ vapor} \\ K_{sink} &= e_{sink} \cdot r_{LWP} \end{aligned} \tag{5}$$

with rates being the product of bulk efficiency coefficients for sources (e_{source}) and sinks (e_{sink}) and their respective reservoir terms. The reservoir that liquid draws from is water vapor ($r_{water\ vapor}$) while the sink reservoir (precipitation) is cloud liquid (r_{LWP}). In the mean-state climate, sources and sinks are balanced ($K_{source} = K_{sink}$) and

$$\frac{e_{source}}{e_{sink}} = \frac{r_{LWP}}{r_{water\ vapor}}. \tag{6}$$

Following this conceptual model, mean-state LWP is proportional to the relative strength of source and sink efficiencies (i.e., e_{source}/e_{sink}). If we assume the same water vapor ($r_{water\ vapor}$) in the mean-state climates of GCMs, the diversity in model mean-state LWP can be traced back to the subgrid-scale parameterization of cloud source and sink processes. Similarity in water vapor climatologies is an assumption, since free-running models without a fixed SST will yield slightly different mean-state water vapor paths (Jiang et al., 2012). In this conceptual model $\partial LWP/\partial P - E$ trained using the GCM mean-state climate may act as a proxy for the relative strength of source to sink efficiencies ($e_{source}/e_{sink} \propto \partial LWP/\partial P - E$).

The steady-state framework outlined here provides insight into why the slope of $\partial LWP/\partial P - E$ for the cold regime is larger than the slope for the warm regime (Figure 5). In this framework, differences in slope could arise due to a stronger source efficiency for cold regime clouds due to the larger moist adiabat (Betts & Harshvardhan, 1987), even though the sink efficiency for cold regime clouds may be larger as well (Field & Heymsfield, 2015)

How does the steady-state framework outlined above inform us of the diversity in the GCM LWP responses to warming? The moisture content ($r_{water\ vapor}$) in the extratropics increases with GMT. If we assume the relative strength of source-to-sink efficiency (e_{source}/e_{sink}) is fixed under climate change, a model with larger mean-state sensitivity of LWP to $P - E$ would simulate a larger increase in LWP. This is consistent with GCM behavior and warm regime $\partial LWP/\partial P - E$ and $\Delta LWP/\Delta GMT$ covary across GCMs (Figure S9 in the supplementary information) with a correlation of $r = 0.78$.

3.3 Constraints on Southern Ocean SW Cloud Feedback

In the proceeding sections we examine the response of SO LWP to GMT predicted by CCFs and the response of α to LWP. Combining these terms in equation 1 we evaluate whether our simplified model of SW_{FB} has skill in predicting GCM SW_{FB}. In Figure 6, we use the $\Delta LWP/\Delta GMT$ and $\partial\alpha/\partial LWP$ calculated from GCMs to predict their SW_{FB} calculated using radiative kernels as presented in Zelinka, Myers, McCoy, Po-Chedley, et al. (2020). The ability of the simple model in equation 1 to reproduce SW_{FB} is evaluated in the $40-50^oS$ and $50-85^oS$ latitude bands (Figure 6). Equation 1 explains 54 % of the variance in GCM SW_{FB} averaged over $40-50^oS$ and and 40 % averaged over $50-85^oS$.

Based on the observational constraints on $\Delta LWP/\Delta GMT$ (Figure 3) and the observational estimate of $\partial\alpha/\partial LWP$ (Figure 5), we provide observational constraints on SW_{FB}. Observational constraints on the right-hand side of equation 1 predict the contributions of $40-50^oS$ and $50-85^oS$ regions' clouds to global mean cloud feedback to be 0.00−0.06 $W\ m^{-2}\ K^{-1}$ and −0.15−0.01 $W\ m^{-2}\ K^{-1}$. These ranges are calculated by taking the shaded y-ranges in Figure 6 and scaling them by the ratio of the area in the latitude band to global surface area. The constraint on $50-85^oS$ SW_{FB} is consistent with the constraint −0.10−0.0 $W\ m^{-2}\ K^{-1}$ calculated by McCoy et al. (2022). The uncertainties in $40-50^oS$ and $50-85^oS$ SW_{FB} constraints are calculated by combining uncertainties in $\Delta LWP/\Delta GMT$ constraints and the uncertainty in the estimate of $\partial\alpha/\partial LWP$. Uncertainties in the constraints on $\Delta LWP/\Delta GMT$ are due to the intermodel spread in $\Delta X/\Delta GMT$ and the uncertainties propagated from the warm regime to latitude bands including both cold and warm regimes (section 3.1.2). The uncertainty in $\partial\alpha/\partial LWP$ is given by varying the clear-sky albedo threshold (section 3.2). The constraint on $40-50^oS$ SW_{FB} is tighter than for $50-85^oS$ because an observational constraint on $\Delta LWP/\Delta GMT$ is only available in the warm regime, and the $40-50^oS$ region is entirely within the warm regime.

To evaluate the extent to which neglecting ice water path (IWP) changes impact our prediction of GCM SW_{FB}, we examined the relative contributions of LWP and IWP changes to SW_{FB} in GCMs. We first calculate the changes in IWP with GMT ($\Delta IWP/\Delta GMT$) between the mean of years 121-140 of $abrupt4xCO_2$ and the average of $piControl$ simulations for all GCMs in this study following the same procedure used in the calculation of $\Delta LWP/\Delta GMT$. The median $\Delta LWP/\Delta GMT$ in $40-85^oS$ is around 10 times larger than $\Delta IWP/\Delta GMT$ across GCMs (Figure S10a). To compare the sensitivity of albedo to LWP ($\partial\alpha/\partial LWP$) with IWP ($\partial\alpha/\partial IWP$), we first partition the TOA albedo (α) into 50 LWP/IWP bins. Then we follow the method for calculating radiative susceptibility (section 2.2.4) to compute the sensitivities of albedo to liquid versus ice by keeping the other variable fixed (Text S2). The product of $\partial\alpha/\partial LWP$ ($\partial\alpha/\partial IWP$) and $\Delta LWP/\Delta GMT$ ($\Delta IWP/\Delta GMT$) is a measure of the contribution of LWP (IWP) changes to the response of α to per degree warming ($\Delta\alpha/\Delta GMT$), which is proportional to their contributions to SW_{FB} (equation 1). Among the GCMs surveyed here, the median contribution to an α response from changes in LWP is inferred to be a factor of 14 larger than that arising from changes in IWP (Figure S10b). This result is consistent with the approximation in equation 1 that the SO SW_{FB} is dominated by LWP changes and the ability of equation 1 to predict the full radiative kernel calculation of SW_{FB}.

We combine our constraints on SW_{FB} for $40-50^oS$ and $50-85^oS$ to compute the constraint on $40-85^oS$ SW_{FB}. We take the sum of the area-weighted latitudinal constraints in $40-50^oS$ and $50-85^oS$ and propagate their standard errors to estimate $40-85^oS$ SW_{FB}. The contribution of the SO clouds to the global mean SW_{FB} is constrained to $-0.168\ -\ 0.051$ $W\ m^{-2}\ K^{-1}$ with a 95% confidence interval (Figure 7). Considering potential systematic error in observations of LWP shifts the constraint on $40-85^oS$ SW_{FB} to $-0.192-0.047$ $W\ m^{-2}\ K^{-1}$. The constrained range of SO SW_{FB} is a bit wider than the range reported by McCoy et al. (2022), but we have added a new constraint from the $40-50^oS$ latitude band and have taken into account the uncertainty in radiative susceptibility arising from different α_{cs} thresholds and potential systematic uncertainties in observed LWP. Our constraint suggests that $40-85^oS$ SW_{FB} is less likely to be extremely negative or positive, as simulated by some CMIP6 GCMs. The most likely range of the SO SW_{FB} is from moderately negative to weakly positive.

4 Conclusions

In this work we built a CCF regression model to predict the response of the SO ($40-85^oS$) LWP to global warming. The CCFs considered in the regression model were surface skin temperature, precipitation minus evaporation (approximately the moisture convergence), lower-tropospheric stability, and 500 mb subsidence. Warm and cold clouds are regulated by very different microphysical processes and have different responses to warming. To allow our CCF regression model to adapt to this, we partitioned the SO into cold and warm regimes. This new method increases the robustness of the CCF model prediction compared to previous work (McCoy et al., 2022). We used two out-of-sample tests to evaluate the predictive ability of our CCF regression model: the ability of our CCF model trained on observations to replicate the observed decadal trend in SO LWP (section 3.1.1; Figure 2) and the ability of our CCF model trained on the mean-state output of GCMs to predict their response to CO_2 quadrupling (section 3.1.2; Figure 3). Using the CCF regression model trained on observations combined with the GCM simulated changes in CCFs in response to CO_2 quadrupling, we were able to provide an observational constraint on the change in LWP in response to GMT ($\Delta LWP/\Delta GMT$) of $2.76 - 4.19\ gm^{-2}K^{-1}$ (Figure 3b).

Ultimately, the quantity we care about in relation to Earth's radiation budget is not cloudiness, but radiative flux. We define a radiative susceptibility to liquid cloud ($\partial\alpha/\partial LWP$) that we can use to scale the LWP changes in response to warming. We compute $\partial\alpha/\partial LWP$ from satellite observations and GCM output. The observational constraint suggests that most of the GCMs overestimate $\partial\alpha/\partial LWP$ (Figure 5), which is consistent with recent studies of tropical clouds (Konsta et al., 2022). Satellite observations estimate $\partial\alpha/\partial LWP$ to be $0.43 - 0.90\ (kg\ m^{-2})^{-1}$.

GCMs with higher mean-state LWP tend to have lower $\partial\alpha/\partial LWP$ (Figure 5)- resulting in compensation between macrophysical changes in cloud and radiative impact. This feature can be connected to the sensitivity of LWP to moisture convergence ($\partial LWP/\partial P - E$). GCMs with higher $\partial LWP/\partial P - E$ simulate higher mean-state LWP. These GCMs tend to predict a larger LWP response ($\Delta LWP/\Delta GMT$) but have a lower $\partial\alpha/\partial LWP$ due to radiative saturation.

Approximating SO SW_{FB} as the product of $\partial\alpha/\partial LWP$ and $\Delta LWP/\Delta GMT$ predicts roughly 50% of the variance in SO SW_{FB} across 50 CMIP5 and CMIP6 GCMs (Table S1) calculated from radiative kernels (Zelinka, Myers, McCoy, Po-Chedley, et al., 2020) (Figure 6). Observational constraints on $\Delta LWP/\Delta GMT$ and $\partial\alpha/\partial LWP$ produce a constrained range on SO SW_{FB} of -0.168 to $0.051\ Wm^{-2}K^{-1}$ (95% confidence interval) (Figure 7), which suggests a moderate negative to weakly positive SO SW_{FB}. This is consistent with previous work (McCoy et al., 2022), but expands the constraint region to the entire SO as opposed to just constraining the region where GCMs consistently moisten and more fully accounts for observational uncertainty.

Our analysis suggests some directions of future studies seeking to constrain extratropical SW_{FB}:

1. Our analysis identified increased moisture convergence into the SO as a key driver of increased LWP. This mechanism ultimately links the global circulation and hydrological cycle to the extratropical SW_{FB}. To better understand this linkage, it would be useful to understand how Hadley cell expansion and transient eddies (i.e. atmospheric rivers) contribute to long-term variability of the SO moisture budget.
2. Due to the lack of microwave observations of LWP over ice, we cannot provide an observationally-constrained CCF model for the cold regime. In this study, the GCM relationship between the warm regime LWP response and the response averaged over the latitude band including both cold and warm regimes provides an estimate

including uncertainty related to the cold regime. Ground-based LWP observations in high latitude SO, such as those taken during the Atmospheric Radiation Measurement (ARM) West Antarctic Radiation Experiment (AWARE, Lubin et al. (2020)), may be able to provide an observational constraint on the cold regime LWP response.

3. We found that $\partial\alpha/\partial LWP$ varied dramatically across GCMs and strongly modulated the effect of changes in LWP on radiation. We also found that observations suggested that GCMs tended to have a $\partial\alpha/\partial LWP$ that was too large. One possibility is that this is due to clouds that are too uniform and radiatively efficient (Konsta et al., 2022; Nam et al., 2012). Determining the origin of this behavior might be helpful in identifying a potential source of GCM bias in SW_{FB}.

5 Open Research

GCM outputs used in this study are available from Earth System Grid Federation (ESGF) esgf-node.llnl.gov (Cinquini et al., 2014)[Data]. The code for calculating the full shortwave cloud feedback data from GCM output is documented and published in (Zelinka, Myers, McCoy, Po-Chedley, et al., 2020) [Software] and at `github.com/mzelinka`. MAC-LWP and MERRA-2 reanalysis data are available from the Goddard Earth Sciences Data and Information Services Center at disc.gsfc.nasa.gov (Elsaesser et al., 2017a; Gelaro, McCarty, Suárez, et al., 2017) [Data]. CERES EBAF Edition 4.1 data is available from ceres.larc.nasa.gov (Loeb et al., 2018a) [Data].

Acknowledgments

The efforts of CT, DTM, and GSE are supported under NASA-PMMST Grant #80NSSC22K0599. GSE acknowledges additional support from the NASA Modeling, Analysis and Prediction Program and APAM GISS Co-Op #80NSSC18M0133. We thank Dr. Mark Zelinka for sharing his shortwave cloud feedback map data for all the GCMs included in this study. We appreciate the World Climate Research Programme (WCRP) for their promoting and coordinating efforts of CMIP. We also thank all modeling groups for producing and publishing their model output. We thank the Earth System Grid Federation (ESGF) for archiving and providing useful accessing tools to all model output, and the multiple funding agencies that support CMIP5/6 and ESGF. We would like to acknowledge the use of computational resources (doi:10.5065/D6RX99HX) at the NCAR-Wyoming Supercomputing Center provided by the National Science Foundation and the State of Wyoming, and supported by NCAR's Computational and Information Systems Laboratory.

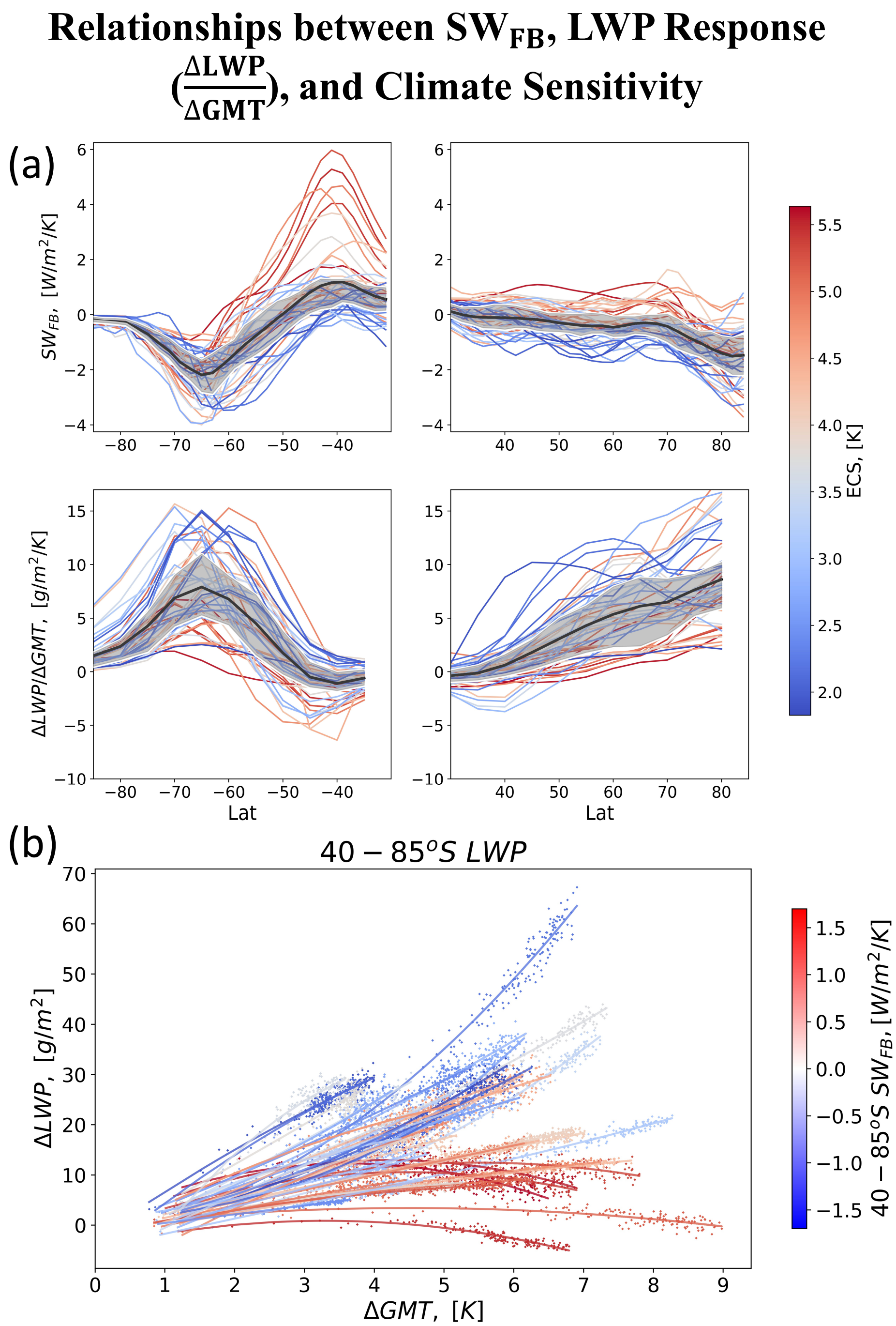

Figure 1. (a) Extratropical SW cloud feedback (SW_{FB}) (top) and the response of liquid water path (LWP) to global-mean temperature (GMT) ($\Delta LWP/\Delta GMT$) in the GCMs in Table S1. Anomalies in LWP and GMT are calculated as the differences between the mean of *piControl* and year 121 - 140's mean of $abrupt4xCO_2$ simulations. Thick black lines are the multi-model mean and the shaded regions correspond to the 25th-75th percentiles of quantities. (b) Annual-mean anomalies in Southern Ocean ($40-85^oS$) averaged LWP versus GMT relative to *piControl* average for the first 150 years of $abrupt4xCO_2$ simulations. Lines show the second-order polynomial fit of the annual-mean LWP responses to GMT for each GCM. Lines for each GCM in (a) and (b) are colored by model effective climate sensitivity (ECS) and the $40 - 85^o$ averaged SW_{FB}, respectively. SW cloud feedback and effective climate sensitivity (ECS) data are from Zelinka, Myers, McCoy, Po-Chedley, et al. (2020).

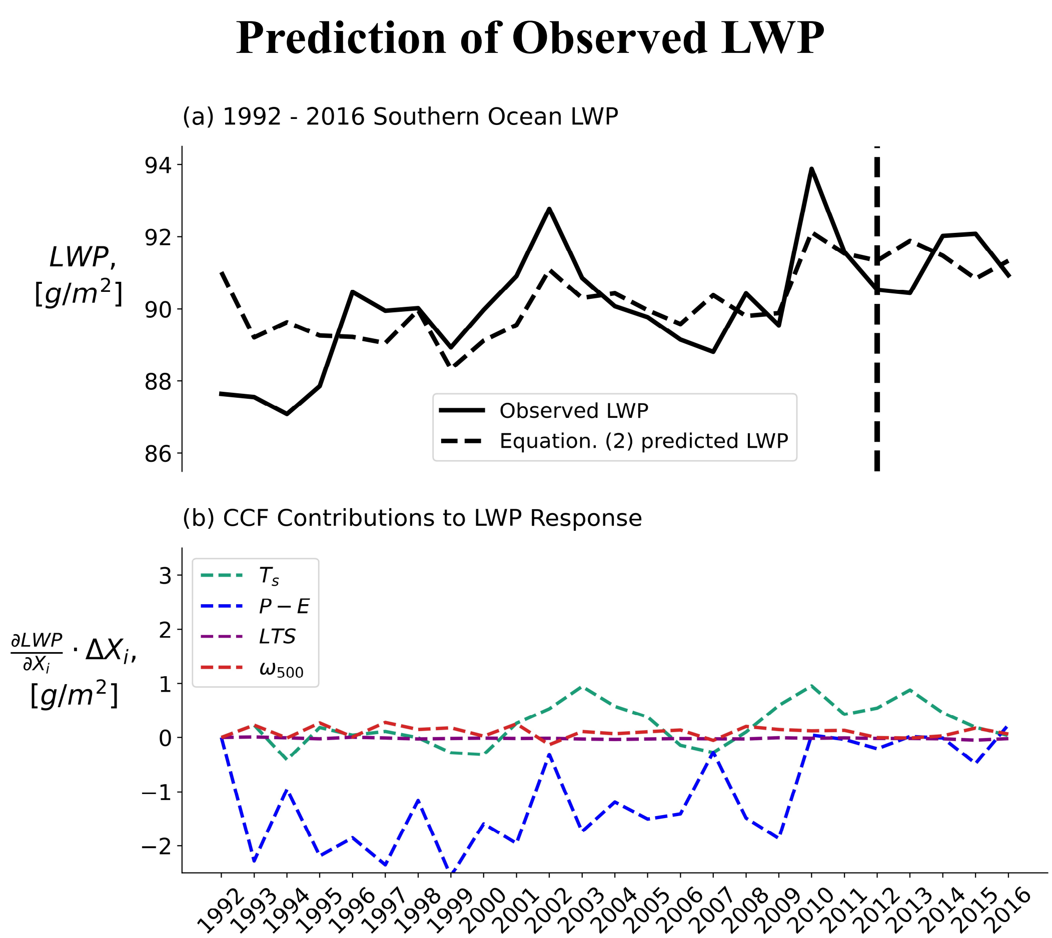

Figure 2. (a) Observed annual-mean Southern Ocean averaged LWP from MAC-LWP (green) and LWP predicted by the CCF model (Equation 2; blue) from 1992 to 2016. The CCF model is trained on monthly-mean data from 2012 to 2016 (right side of the dashed line) and is used to predict the annual-mean LWP back to 1992. (b) The decomposition of annual-mean LWP anomalies into individual CCF contributions by equation 2.

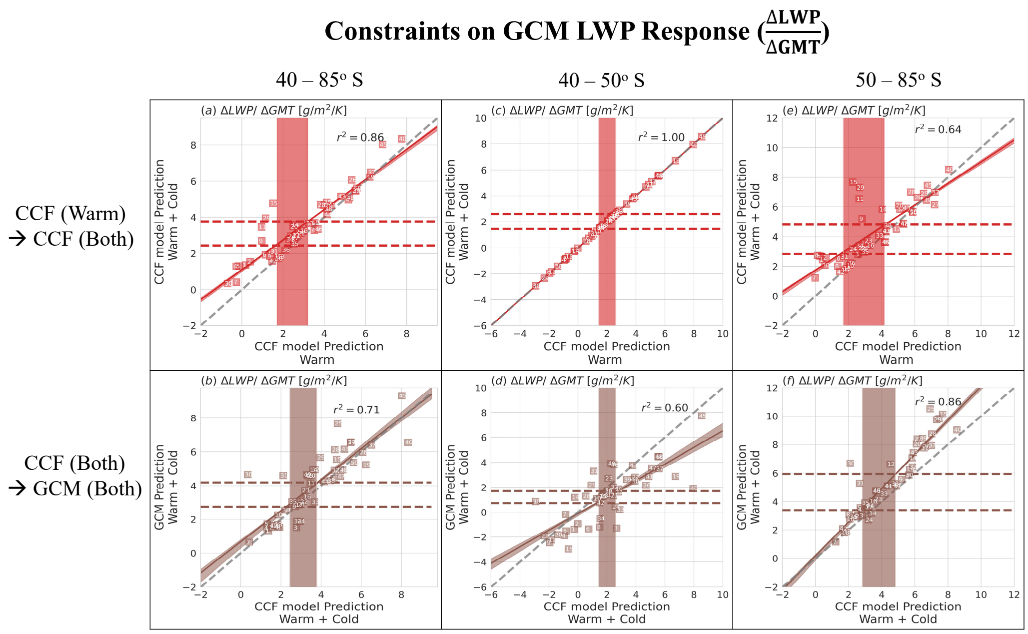

Figure 3. Predictions of the GCM-simulated LWP response to CO_2 quadrupling ($\Delta LWP/\Delta GMT$) by Equation 3. $\Delta LWP/\Delta GMT$ is shown averaged over (a,b) $40-85^oS$, (c,d) $40-50^oS$, and (e,f): $50-85^oS$. (a,c,e) Latitude-averaged $\Delta LWP/\Delta GMT$ predicted by equation 3 in warm and cold regimes versus only in the warm regime. (b,d,f) Latitude-averaged $\Delta LWP/\Delta GMT$ simulated by GCMs versus $\Delta LWP/\Delta GMT$ predicted by equation 3 in both regimes. 1-1 lines are shown using dashed gray lines and best-fit lines are shown as solid red and brown lines with their uncertainties estimated by Jackknife resampling. Observational constraints (red shading) are shown in (a,c,e). This constraint is propagated from the warm regime $\Delta LWP/\Delta GMT$ to the $\Delta LWP/\Delta GMT$ in both regimes by taking the intersection between the red shading and the best-fit line with its uncertainty (red dashed lines). Constraints on $\Delta LWP/\Delta GMT$ in both regimes are then shown in (b,d,f) using brown shading. The constrained ranges are combined with the uncertainty in the CCF model prediction by using the best-fit line between GCM and CCF model predictions to yield an observational constraint on GCM-simulated $\Delta LWP/\Delta GMT$ (brown dashed lines). Explained variance (r^2) is shown in each subplot. GCMs are denoted with the number listed in Table S1.

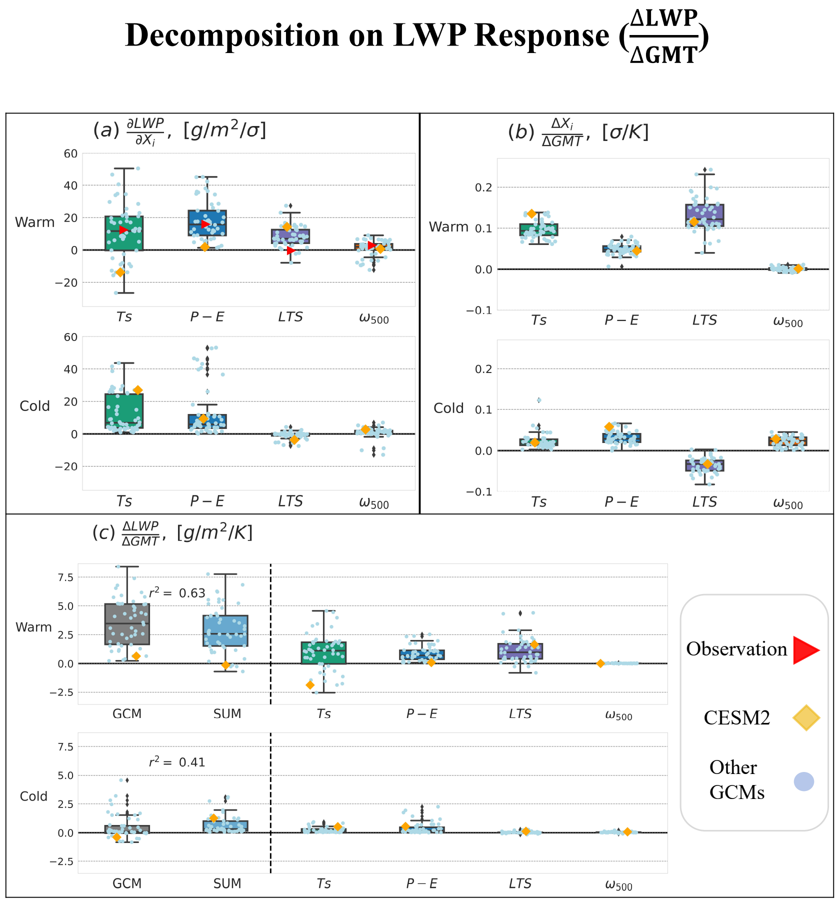

Figure 4. Decomposition of $\Delta LWP/\Delta GMT$ predicted by Equation 3: (a) Sensitivities of LWP each CCF; (b) standardized change in each CCF per degree warming; (c) LWP changes due to each CCF (the product of (a) with (b)), their sum (sky blue box), and the GCM-simulated LWP response (gray box). Cold and Warm regime values are shown separately. The variance (r^2) of GCM-simulated $\Delta LWP/\Delta GMT$ explained by the CCF model predictions in each regime is shown in subplot (c). Changes in CCFs are normalized by their spatio-temporal standard deviations of each regime in the mean-state climate. We single out one GCM, CESM2, by denoting its values as orange diamonds. All other GCMs are denoted as light blue dots. Observational sensitivities are denoted as red triangles in the warm regime.

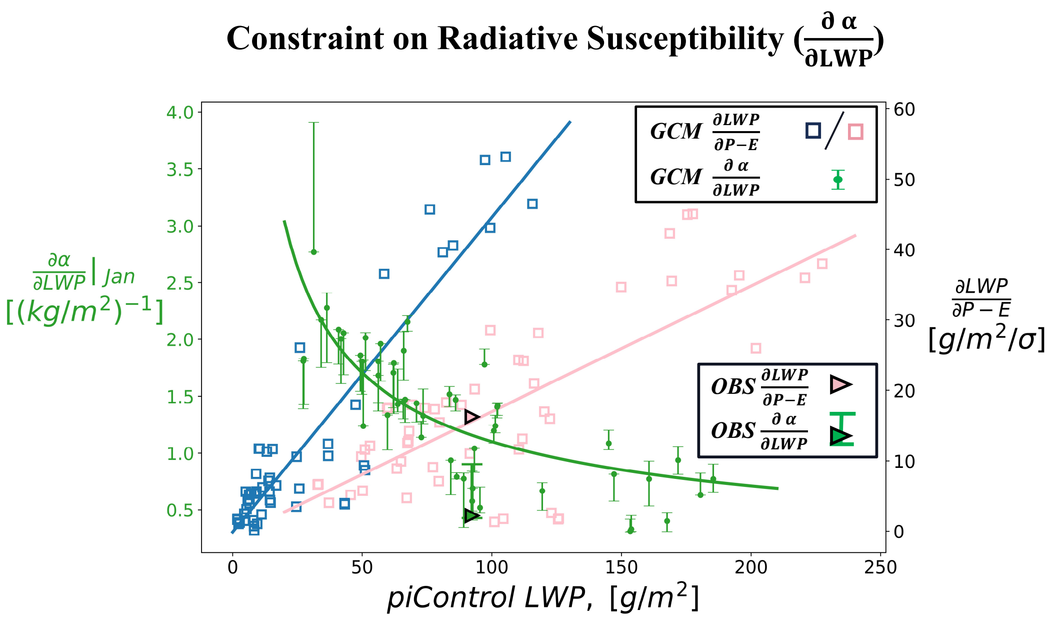

Figure 5. The radiative susceptibility ($\partial\alpha/\partial LWP$, left axis) and the sensitivity of LWP to moisture convergence ($\partial LWP/\partial P-E$, right axis) in the warm (pink) and cold (blue) regimes as a function of regime mean-state (*piControl*) LWP. Observed $\partial LWP/\partial P-E$ and $\partial\alpha/\partial LWP$ are shown by the pink and green triangles (observational $\partial LWP/\partial P-E$ is comparable to the warm regime values of GCMs for reason discussed in sections 2.1 and 2.2.3). The linear fit between $\partial LWP/\partial P-E$ and *piControl* LWP in each regime and the power law fit between $\partial\alpha/\partial LWP$ and *piControl* LWP are shown. Uncertainty in $\partial\alpha/\partial LWP$ from varying the maximum clear-sky albedo $TR_{\alpha_{cs}}$ from 0.11 to 0.30 is shown as an uncertainty range.

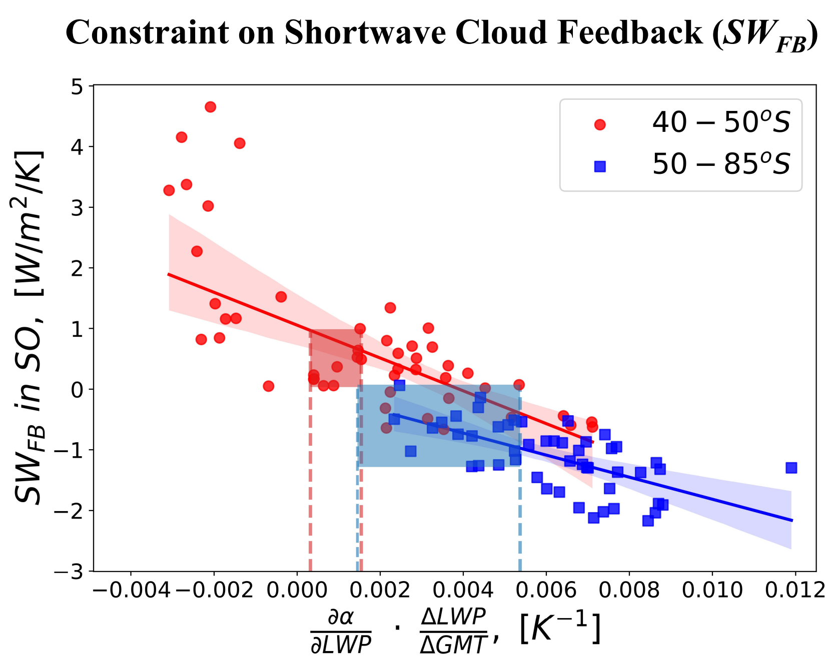

Figure 6. The SW cloud feedback of GCMs listed in Table S1 from Zelinka, Myers, McCoy, Po-Chedley, et al. (2020) for $40-50^oS$ (red) and $50-85^oS$ (blue) latitude bands versus predictions from the simplified physical model developed in this study (Equation 1). The observational constraints on $40-50^oS$ and $50-85^oS$ the constrained ranges on the y-axis of Figure 3 (d) and (f). The observational constraint on radiative susceptibilities ($\partial\alpha/\partial LWP$) is the error range of the green triangle in Figure 5. The combination of these two constraints yields constraints on $40-50^oS$ and $50-85^oS$ SW_{FB}, shown as shaded regions along the x-axis. Constrained $40-50^oS$ and $50-85^oS$ SW_{FB} are the extents of y-coordinate of models within the shaded regions. The linear fit between model SW_{FB} and predictions from equation 1 are shown with their 95% confidence interval.

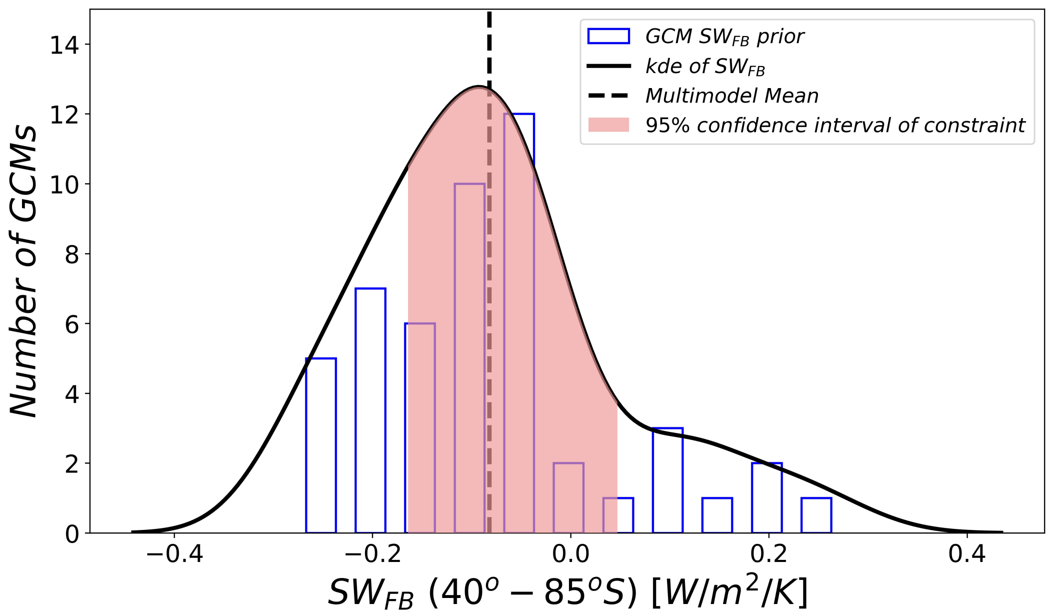

Figure 7. The contribution of Southern Ocean ($40 - 85^oS$) SW_{FB} to the global mean cloud feedback. The prior distribution of SW_{FB} for GCMs listed in Table S1 is shown as the blue histograms and black kernel density estimate. The dashed black line denotes the multimodel mean of SW_{FB} for 50 GCMs. Red shading shows the 95% confidence interval of the Southern Ocean ($40 - 85^oS$) averaged SW_{FB} by combining the constrained $40 - 50^oS$ and $50 - 85^oS$ averaged SW_{FB} shown in Figure 6. Observational constraint suggests a moderate negative to weak positive Southern Ocean SW_{FB}.

References

Allen, M. R., & Ingram, W. J. (2002, September). Constraints on future changes in climate and the hydrologic cycle. *Nature*, *419*(6903), 224–232. Retrieved 2023-02-27, from https://www.nature.com/articles/nature01092 doi: 10.1038/nature01092

Andrews, T., Gregory, J. M., Webb, M. J., & Taylor, K. E. (2012, May). Forcing, feedbacks and climate sensitivity in CMIP5 coupled atmosphere-ocean climate models: CLIMATE SENSITIVITY IN CMIP5 MODELS. *Geophysical Research Letters*, *39*(9), n/a–n/a. Retrieved 2021-11-16, from http://doi.wiley.com/10.1029/2012GL051607 doi: 10.1029/2012GL051607

Barnes, E. A., & Polvani, L. (2013, September). Response of the Midlatitude Jets, and of Their Variability, to Increased Greenhouse Gases in the CMIP5 Models. *Journal of Climate*, *26*(18), 7117–7135. Retrieved 2023-01-31, from http://journals.ametsoc.org/doi/10.1175/JCLI-D-12-00536.1 doi: 10.1175/JCLI-D-12-00536.1

Bender, F. A.-M., Engström, A., Wood, R., & Charlson, R. J. (2017, June). Evaluation of Hemispheric Asymmetries in Marine Cloud Radiative Properties. *Journal of Climate*, *30*(11), 4131–4147. Retrieved 2022-06-14, from http://journals.ametsoc.org/doi/10.1175/JCLI-D-16-0263.1 doi: 10.1175/JCLI-D-16-0263.1

Bender, F. A.-M., Ramanathan, V., & Tselioudis, G. (2012, May). Changes in extratropical storm track cloudiness 1983–2008: observational support for a poleward shift. *Climate Dynamics*, *38*(9-10), 2037–2053. Retrieved 2022-04-04, from http://link.springer.com/10.1007/s00382-011-1065-6 doi: 10.1007/s00382-011-1065-6

Betts, A. K., & Harshvardhan. (1987). Thermodynamic constraint on the cloud liquid water feedback in climate models. *Journal of Geophysical Research*, *92*(D7), 8483. Retrieved 2022-05-20, from http://doi.wiley.com/10.1029/JD092iD07p08483 doi: 10.1029/JD092iD07p08483

Bjordal, J., Storelvmo, T., Alterskjær, K., & Carlsen, T. (2020, November). Equilibrium climate sensitivity above 5 °C plausible due to state-dependent cloud feedback. *Nature Geoscience*, *13*(11), 718–721. Retrieved 2022-05-20, from https://www.nature.com/articles/s41561-020-00649-1 doi: 10.1038/s41561-020-00649-1

Bodas-Salcedo, A., Webb, M. J., Bony, S., Chepfer, H., Dufresne, J.-L., Klein, S. A., … John, V. O. (2011, August). COSP: Satellite simulation software for model assessment. *Bulletin of the American Meteorological Society*, *92*(8), 1023–1043. Retrieved 2022-05-20, from https://journals.ametsoc.org/doi/10.1175/2011BAMS2856.1 doi: 10.1175/2011BAMS2856.1

Bodas-Salcedo, A., Mulcahy, J. P., Andrews, T., Williams, K. D., Ringer, M. A., Field, P. R., & Elsaesser, G. S. (2019, June). Strong Dependence of Atmospheric Feedbacks on Mixed-Phase Microphysics and Aerosol-Cloud Interactions in HadGEM3. *Journal of Advances in Modeling Earth Systems*, *11*(6), 1735–1758. Retrieved 2023-01-26, from https://onlinelibrary.wiley.com/doi/10.1029/2019MS001688 doi: 10.1029/2019MS001688

Bonan, D. B., Siler, N., Roe, G. H., & Armour, K. C. (2023, February). Energetic constraints on the pattern of changes to the hydrological cycle under global warming. *Journal of Climate*, 1–48. Retrieved 2023-02-24, from https://journals.ametsoc.org/view/journals/clim/aop/JCLI-D-22-0337.1/JCLI-D-22-0337.1.xml doi: 10.1175/JCLI-D-22-0337.1

Bony, S., Colman, R., Kattsov, V. M., Allan, R. P., Bretherton, C. S., Dufresne, J.-L., … Webb, M. J. (2006, August). How Well Do We Understand and Evaluate Climate Change Feedback Processes? *Journal of Climate*, *19*(15), 3445–3482. Retrieved 2023-08-17, from http://journals.ametsoc.org/doi/10.1175/JCLI3819.1 doi: 10.1175/JCLI3819.1

Boucher, O., & el. (2014). *Climate Change 2013 – The Physical Science Basis: Working Group I Contribution to the Fifth Assessment Report of the Intergovernmental Panel on Climate Change* (1st ed.). Cambridge University Press. Retrieved 2023-08-24, from https://www.cambridge.org/core/product/identifier/9781107415324/type/book doi: 10.1017/CBO9781107415324

Bretherton, C. S., Blossey, P. N., & Jones, C. R. (2013, June). Mechanisms of marine low cloud sensitivity to idealized climate perturbations: A single-LES exploration extending the CGILS cases. *Journal of Advances in Modeling Earth Systems*, *5*(2), 316–337. Retrieved 2022-04-02, from https://onlinelibrary.wiley.com/doi/10.1002/jame.20019 doi: 10.1002/jame.20019

Bretherton, C. S., & Wyant, M. C. (1997, January). Moisture Transport, Lower-Tropospheric Stability, and Decoupling of Cloud-Topped Boundary Layers. *Journal of the Atmospheric Sciences*, *54*(1), 148–167. Retrieved 2022-11-17, from http://journals.ametsoc.org/doi/10.1175/1520-0469(1997)054<0148:MTLTSA>2.0.CO;2 doi: 10.1175/1520-0469(1997)054⟨0148:MTLTSA⟩2.0.CO;2

Brient, F., & Schneider, T. (2016, August). Constraints on Climate Sensitivity from Space-Based Measurements of Low-Cloud Reflection. *Journal of Climate*, *29*(16), 5821–5835. Retrieved 2023-01-22, from http://journals.ametsoc.org/doi/10.1175/JCLI-D-15-0897.1 doi: 10.1175/JCLI-D-15-0897.1

Ceppi, P., Hartmann, D. L., & Webb, M. J. (2016, January). Mechanisms of the Negative Shortwave Cloud Feedback in Middle to High Latitudes. *Journal of Climate*, *29*(1), 139–157. Retrieved 2023-02-22, from http://journals.ametsoc.org/doi/10.1175/JCLI-D-15-0327.1 doi: 10.1175/JCLI-D-15-0327.1

Ceppi, P., McCoy, D. T., & Hartmann, D. L. (2016, February). Observational evidence for a negative shortwave cloud feedback in middle to high latitudes. *Geophysical Research Letters*, *43*(3), 1331–1339. Retrieved 2023-02-04, from https://onlinelibrary.wiley.com/doi/10.1002/2015GL067499 doi: 10.1002/2015GL067499

Cesana, G., Del Genio, A. D., Ackerman, A. S., Kelley, M., Elsaesser, G., Fridlind, A. M., … Yao, M.-S. (2019, March). Evaluating models' response of tropical low clouds to SST forcings using CALIPSO observations. *Atmospheric Chemistry and Physics*, *19*(5), 2813–2832. Retrieved 2022-04-03, from https://acp.copernicus.org/articles/19/2813/2019/ doi: 10.5194/acp-19-2813-2019

Cesana, G. V., & Del Genio, A. D. (2021, March). Observational constraint on cloud feedbacks suggests moderate climate sensitivity. *Nature Climate Change*, *11*(3), 213–218. Retrieved 2022-04-08, from http://www.nature.com/articles/s41558-020-00970-y doi: 10.1038/s41558-020-00970-y

Cinquini, L., Crichton, D., Mattmann, C., Harney, J., Shipman, G., Wang, F., … others (2014). *The earth system grid federation: An open infrastructure for access to distributed geospatial data* (Vol. 36) [dataset]. Elsevier.

Danabasoglu, G., Lamarque, J., Bacmeister, J., Bailey, D. A., DuVivier, A. K., Edwards, J., … Strand, W. G. (2020, February). The Community Earth System Model Version 2 (CESM2). *Journal of Advances in Modeling Earth Systems*, *12*(2). Retrieved 2023-03-30, from https://onlinelibrary.wiley.com/doi/10.1029/2019MS001916 doi: 10.1029/2019MS001916

Elsaesser, G. S., O'Dell, C. W., Lebsock, M. D., Bennartz, R., Greenwald, T. J., & Wentz, F. J. (2017a). *The multisensor advanced climatology of liquid water path (mac-lwp)* (Vol. 30) (dataset No. 24). American Meteorological Society.

Elsaesser, G. S., O'Dell, C. W., Lebsock, M. D., Bennartz, R., Greenwald, T. J., & Wentz, F. J. (2017b, December). The Multisensor Advanced Climatology of Liquid Water Path (MAC-LWP). *Journal of Climate*, *30*(24), 10193–10210.

Retrieved 2022-09-06, from https://journals.ametsoc.org/doi/10.1175/JCLI-D-16-0902.1 doi: 10.1175/JCLI-D-16-0902.1

Field, P. R., & Heymsfield, A. J. (2015, November). Importance of snow to global precipitation. *Geophysical Research Letters*, *42*(21), 9512–9520. Retrieved 2023-03-22, from https://onlinelibrary.wiley.com/doi/10.1002/2015GL065497 doi: 10.1002/2015GL065497

Field, P. R., & Wood, R. (2007, January). Precipitation and Cloud Structure in Midlatitude Cyclones. *Journal of Climate*, *20*(2), 233–254. Retrieved 2023-10-18, from http://journals.ametsoc.org/doi/10.1175/JCLI3998.1 doi: 10.1175/JCLI3998.1

Forster, P., & el. (2023). *Climate Change 2021 – The Physical Science Basis: Working Group I Contribution to the Sixth Assessment Report of the Intergovernmental Panel on Climate Change* (1st ed.). Cambridge University Press. Retrieved 2023-08-23, from https://www.cambridge.org/core/product/identifier/9781009157896/type/book doi: 10.1017/9781009157896.009

Frazer, M. E., & Ming, Y. (2022, April). Understanding the Extratropical Liquid Water Path Feedback in Mixed-Phase Clouds with an Idealized Global Climate Model. *Journal of Climate*, *35*(8), 2391–2406. Retrieved 2023-01-26, from https://journals.ametsoc.org/view/journals/clim/35/8/JCLI-D-21-0334.1.xml doi: 10.1175/JCLI-D-21-0334.1

Frey, W. R., & Kay, J. E. (2018, April). The influence of extratropical cloud phase and amount feedbacks on climate sensitivity. *Climate Dynamics*, *50*(7-8), 3097–3116. Retrieved 2023-07-05, from http://link.springer.com/10.1007/s00382-017-3796-5 doi: 10.1007/s00382-017-3796-5

Gelaro, R., McCarty, W., Suárez, M. J., Todling, R., Molod, A., Takacs, L., … others (2017). *The modern-era retrospective analysis for research and applications, version 2 (merra-2)* (Vol. 30) (dataset No. 14).

Gelaro, R., McCarty, W., Suárez, M. J., Todling, R., Molod, A., Takacs, L., … Zhao, B. (2017, July). The Modern-Era Retrospective Analysis for Research and Applications, Version 2 (MERRA-2). *Journal of Climate*, *30*(14), 5419–5454. Retrieved 2023-03-29, from https://journals.ametsoc.org/doi/10.1175/JCLI-D-16-0758.1 doi: 10.1175/JCLI-D-16-0758.1

Gettelman, A., Hannay, C., Bacmeister, J. T., Neale, R. B., Pendergrass, A. G., Danabasoglu, G., … Mills, M. J. (2019, July). High Climate Sensitivity in the Community Earth System Model Version 2 (CESM2). *Geophysical Research Letters*, *46*(14), 8329–8337. Retrieved 2023-02-02, from https://onlinelibrary.wiley.com/doi/10.1029/2019GL083978 doi: 10.1029/2019GL083978

Golaz, J., Caldwell, P. M., Van Roekel, L. P., Petersen, M. R., Tang, Q., Wolfe, J. D., … Zhu, Q. (2019, July). The DOE E3SM Coupled Model Version 1: Overview and Evaluation at Standard Resolution. *Journal of Advances in Modeling Earth Systems*, *11*(7), 2089–2129. Retrieved 2023-08-17, from https://onlinelibrary.wiley.com/doi/abs/10.1029/2018MS001603 doi: 10.1029/2018MS001603

Gordon, N. D., & Klein, S. A. (2014, May). Low-cloud optical depth feedback in climate models: Optical Depth Feedback. *Journal of Geophysical Research: Atmospheres*, *119*(10), 6052–6065. Retrieved 2022-03-29, from http://doi.wiley.com/10.1002/2013JD021052 doi: 10.1002/2013JD021052

Greenwald, T. J., Bennartz, R., Lebsock, M., & Teixeira, J. (2018, April). An Uncertainty Data Set for Passive Microwave Satellite Observations of Warm Cloud Liquid Water Path. *Journal of Geophysical Research: Atmospheres*, *123*(7), 3668–3687. Retrieved 2023-06-23, from https://onlinelibrary.wiley.com/doi/10.1002/2017JD027638 doi: 10.1002/2017JD027638

Grise, K. M., & Medeiros, B. (2016, December). Understanding the Varied Influence of Midlatitude Jet Position on Clouds and Cloud Radiative Effects in Observations and Global Climate Models. *Journal of Climate*, *29*(24), 9005–9025. Retrieved 2022-04-03, from http://journals.ametsoc.org/doi/10.1175/JCLI-D-16-0295.1 doi: 10.1175/JCLI-D-16-0295.1

Haynes, J. M., Jakob, C., Rossow, W. B., Tselioudis, G., & Brown, J. (2011, October). Major Characteristics of Southern Ocean Cloud Regimes and Their Effects on the Energy Budget. *Journal of Climate*, *24*(19), 5061–5080. Retrieved 2022-04-03, from https://journals.ametsoc.org/doi/10.1175/2011JCLI4052.1 doi: 10.1175/2011JCLI4052.1

Held, I. M., & Soden, B. J. (2006, November). Robust Responses of the Hydrological Cycle to Global Warming. *Journal of Climate*, *19*(21), 5686–5699. Retrieved 2022-09-02, from http://journals.ametsoc.org/doi/10.1175/JCLI3990.1 doi: 10.1175/JCLI3990.1

Houghton, J. T., & el. (2001). *Climate change 2001: the scientific basis: contribution of Working Group I to the third assessment report of the Intergovernmental Panel on Climate Change.* Cambridge ; New York: Cambridge University Press.

Huang, Y., Xia, Y., & Tan, X. (2017, October). On the pattern of CO_2 radiative forcing and poleward energy transport: CO_2 Forcing Pattern and Energy Transport. *Journal of Geophysical Research: Atmospheres*, *122*(20), 10,578–10,593. Retrieved 2023-07-13, from http://doi.wiley.com/10.1002/2017JD027221 doi: 10.1002/2017JD027221

Jiang, J. H., Su, H., Zhai, C., Perun, V. S., Del Genio, A., Nazarenko, L. S., ... Stephens, G. L. (2012, July). Evaluation of cloud and water vapor simulations in CMIP5 climate models using NASA "A-Train" satellite observations: EVALUATION OF IPCC AR5 MODEL SIMULATIONS. *Journal of Geophysical Research: Atmospheres*, *117*(D14), n/a–n/a. Retrieved 2023-02-03, from http://doi.wiley.com/10.1029/2011JD017237 doi: 10.1029/2011JD017237

Klein, S. A., Hall, A., Norris, J. R., & Pincus, R. (2017, November). Low-Cloud Feedbacks from Cloud-Controlling Factors: A Review. *Surveys in Geophysics*, *38*(6), 1307–1329. Retrieved 2021-06-21, from http://link.springer.com/10.1007/s10712-017-9433-3 doi: 10.1007/s10712-017-9433-3

Klein, S. A., & Hartmann, D. L. (1993, August). The Seasonal Cycle of Low Stratiform Clouds. *Journal of Climate*, *6*(8), 1587–1606. Retrieved 2023-03-12, from http://journals.ametsoc.org/doi/10.1175/1520-0442(1993)006<1587:TSCOLS>2.0.CO;2 doi: 10.1175/1520-0442(1993)006⟨1587:TSCOLS⟩2.0.CO;2

Komurcu, M., Storelvmo, T., Tan, I., Lohmann, U., Yun, Y., Penner, J. E., ... Takemura, T. (2014, March). Intercomparison of the cloud water phase among global climate models: CLOUD WATER PHASE IN GCMs. *Journal of Geophysical Research: Atmospheres*, *119*(6), 3372–3400. Retrieved 2023-03-23, from http://doi.wiley.com/10.1002/2013JD021119 doi: 10.1002/2013JD021119

Konsta, D., Dufresne, J., Chepfer, H., Vial, J., Koshiro, T., Kawai, H., ... Ogura, T. (2022, June). Low-Level Marine Tropical Clouds in Six CMIP6 Models Are Too Few, Too Bright but Also Too Compact and Too Homogeneous. *Geophysical Research Letters*, *49*(11). Retrieved 2023-03-30, from https://onlinelibrary.wiley.com/doi/10.1029/2021GL097593 doi: 10.1029/2021GL097593

Lacis, A. A., & Hansen, J. (1974, January). A Parameterization for the Absorption of Solar Radiation in the Earth's Atmosphere. *Journal of the Atmospheric Sciences*, *31*(1), 118–133. Retrieved 2023-03-30, from http://journals.ametsoc.org/doi/10.1175/1520-0469(1974)031<0118:APFTAO>2.0.CO;2 doi: 10.1175/1520-0469(1974)031⟨0118:APFTAO⟩2.0.CO;2

Liou, K.-N. (2002). *An introduction to atmospheric radiation* (2nd ed ed.). Amsterdam: Academic Press. (OCLC: 156781712)

Loeb, N. G., Doelling, D. R., Wang, H., Su, W., Nguyen, C., Corbett, J. G., ... Kato, S. (2018a). *Clouds and the earth's radiant energy system (ceres) energy balanced and filled (ebaf) top-of-atmosphere (toa) edition-4.0 data product* (Vol. 31) (dataset No. 2).

Loeb, N. G., Doelling, D. R., Wang, H., Su, W., Nguyen, C., Corbett, J. G., ... Kato, S. (2018b, January). Clouds and the Earth's Radiant Energy System (CERES) Energy Balanced and Filled (EBAF) Top-of-Atmosphere (TOA) Edition-4.0 Data Product. *Journal of Climate*, *31*(2), 895–918. Retrieved 2023-01-19, from `https://journals.ametsoc.org/doi/10.1175/JCLI-D-17-0208.1` doi: 10.1175/JCLI-D-17-0208.1

Loeb, N. G., Rose, F. G., Kato, S., Rutan, D. A., Su, W., Wang, H., ... Gettelman, A. (2020, January). Toward a Consistent Definition between Satellite and Model Clear-Sky Radiative Fluxes. *Journal of Climate*, *33*(1), 61–75. Retrieved 2023-08-09, from `http://journals.ametsoc.org/doi/10.1175/JCLI-D-19-0381.1` doi: 10.1175/JCLI-D-19-0381.1

Lorenz, D. J., & DeWeaver, E. T. (2007, July). The Response of the Extratropical Hydrological Cycle to Global Warming. *Journal of Climate*, *20*(14), 3470–3484. Retrieved 2023-04-19, from `http://journals.ametsoc.org/doi/10.1175/JCLI4192.1` doi: 10.1175/JCLI4192.1

Lubin, D., Zhang, D., Silber, I., Scott, R. C., Kalogeras, P., Battaglia, A., ... Vogelmann, A. M. (2020, July). AWARE: The Atmospheric Radiation Measurement (ARM) West Antarctic Radiation Experiment. *Bulletin of the American Meteorological Society*, *101*(7), E1069–E1091. Retrieved 2023-04-13, from `https://journals.ametsoc.org/view/journals/bams/101/7/bamsD180278.xml` doi: 10.1175/BAMS-D-18-0278.1

Manaster, A., O'Dell, C. W., & Elsaesser, G. (2017, August). Evaluation of Cloud Liquid Water Path Trends Using a Multidecadal Record of Passive Microwave Observations. *Journal of Climate*, *30*(15), 5871–5884. Retrieved 2023-01-24, from `https://journals.ametsoc.org/doi/10.1175/JCLI-D-16-0399.1` doi: 10.1175/JCLI-D-16-0399.1

Marchand, R., Haynes, J., Mace, G. G., Ackerman, T., & Stephens, G. (2009, January). A comparison of simulated cloud radar output from the multiscale modeling framework global climate model with CloudSat cloud radar observations. *Journal of Geophysical Research*, *114*, D00A20. Retrieved 2023-08-24, from `http://doi.wiley.com/10.1029/2008JD009790` doi: 10.1029/2008JD009790

McCoy, D. T., Eastman, R., Hartmann, D. L., & Wood, R. (2017, May). The Change in Low Cloud Cover in a Warmed Climate Inferred from AIRS, MODIS, and ERA-Interim. *Journal of Climate*, *30*(10), 3609–3620. Retrieved 2022-03-27, from `http://journals.ametsoc.org/doi/10.1175/JCLI-D-15-0734.1` doi: 10.1175/JCLI-D-15-0734.1

McCoy, D. T., Field, P., Bodas-Salcedo, A., Elsaesser, G. S., & Zelinka, M. D. (2020, December). A Regime-Oriented Approach to Observationally Constraining Extratropical Shortwave Cloud Feedbacks. *Journal of Climate*, *33*(23), 9967–9983. Retrieved 2020-11-29, from `https://journals.ametsoc.org/jcli/article/33/23/9967/354498/A-Regime-Oriented-Approach-to-Observationally` (Publisher: American Meteorological Society) doi: 10.1175/JCLI-D-19-0987.1

McCoy, D. T., Field, P., Frazer, M. E., Zelinka, M. D., Elsaesser, G. S., Mülmenstädt, J., ... Lebo, Z. J. (2022, April). Extratropical Shortwave Cloud Feedbacks in the Context of the Global Circulation and Hydrological Cycle. *Geophysical Research Letters*, *49*(8). Retrieved 2022-09-13, from `https://onlinelibrary.wiley.com/doi/10.1029/2021GL097154` doi: 10.1029/2021GL097154

McCoy, D. T., Field, P., Gordon, H., Elsaesser, G. S., & Grosvenor, D. P. (2020, April). Untangling causality in midlatitude aerosol–cloud adjustments. *Atmospheric Chemistry and Physics*, *20*(7), 4085–4103. Retrieved 2023-04-13, from https://acp.copernicus.org/articles/20/4085/2020/ doi: 10.5194/acp-20-4085-2020

McCoy, D. T., Field, P. R., Elsaesser, G. S., Bodas-Salcedo, A., Kahn, B. H., Zelinka, M. D., … Wilkinson, J. (2019, January). Cloud feedbacks in extratropical cyclones: insight from long-term satellite data and high-resolution global simulations. *Atmospheric Chemistry and Physics*, *19*(2), 1147–1172. Retrieved 2022-09-02, from https://acp.copernicus.org/articles/19/1147/2019/ doi: 10.5194/acp-19-1147-2019

McCoy, D. T., Field, P. R., Schmidt, A., Grosvenor, D. P., Bender, F. A.-M., Shipway, B. J., … Elsaesser, G. S. (2018, April). Aerosol midlatitude cyclone indirect effects in observations and high-resolution simulations. *Atmospheric Chemistry and Physics*, *18*(8), 5821–5846. Retrieved 2022-05-20, from https://acp.copernicus.org/articles/18/5821/2018/ doi: 10.5194/acp-18-5821-2018

McCoy, D. T., Hartmann, D. L., & Grosvenor, D. P. (2014, December). Observed Southern Ocean Cloud Properties and Shortwave Reflection. Part II: Phase Changes and Low Cloud Feedback*. *Journal of Climate*, *27*(23), 8858–8868. Retrieved 2022-12-21, from http://journals.ametsoc.org/doi/10.1175/JCLI-D-14-00288.1 doi: 10.1175/JCLI-D-14-00288.1

McCoy, D. T., Tan, I., Hartmann, D. L., Zelinka, M. D., & Storelvmo, T. (2016, June). On the relationships among cloud cover, mixed-phase partitioning, and planetary albedo in GCMs. *Journal of Advances in Modeling Earth Systems*, *8*(2), 650–668. Retrieved 2022-06-14, from https://onlinelibrary.wiley.com/doi/10.1002/2015MS000589 doi: 10.1002/2015MS000589

Morrison, H., de Boer, G., Feingold, G., Harrington, J., Shupe, M. D., & Sulia, K. (2012, January). Resilience of persistent Arctic mixed-phase clouds. *Nature Geoscience*, *5*(1), 11–17. Retrieved 2023-02-07, from http://www.nature.com/articles/ngeo1332 doi: 10.1038/ngeo1332

Myers, T. A., & Norris, J. R. (2013, October). Observational Evidence That Enhanced Subsidence Reduces Subtropical Marine Boundary Layer Cloudiness. *Journal of Climate*, *26*(19), 7507–7524. Retrieved 2021-12-06, from http://journals.ametsoc.org/doi/10.1175/JCLI-D-12-00736.1 doi: 10.1175/JCLI-D-12-00736.1

Myers, T. A., & Norris, J. R. (2015, April). On the Relationships between Subtropical Clouds and Meteorology in Observations and CMIP3 and CMIP5 Models*. *Journal of Climate*, *28*(8), 2945–2967. Retrieved 2023-04-13, from http://journals.ametsoc.org/doi/10.1175/JCLI-D-14-00475.1 doi: 10.1175/JCLI-D-14-00475.1

Myers, T. A., & Norris, J. R. (2016, March). Reducing the uncertainty in subtropical cloud feedback. *Geophysical Research Letters*, *43*(5), 2144–2148. Retrieved 2021-12-06, from https://onlinelibrary.wiley.com/doi/10.1002/2015GL067416 doi: 10.1002/2015GL067416

Myers, T. A., Scott, R. C., Zelinka, M. D., Klein, S. A., Norris, J. R., & Caldwell, P. M. (2021, June). Observational constraints on low cloud feedback reduce uncertainty of climate sensitivity. *Nature Climate Change*, *11*(6), 501–507. Retrieved 2021-06-21, from http://www.nature.com/articles/s41558-021-01039-0 doi: 10.1038/s41558-021-01039-0

Nam, C., Bony, S., Dufresne, J.-L., & Chepfer, H. (2012, November). The 'too few, too bright' tropical low-cloud problem in CMIP5 models: TOO FEW TOO BRIGHT LOW-CLOUDS. *Geophysical Research Letters*, *39*(21), n/a–n/a. Retrieved 2023-03-30, from http://doi.wiley.com/10.1029/2012GL053421 doi: 10.1029/2012GL053421

Norris, J. R., Allen, R. J., Evan, A. T., Zelinka, M. D., O'Dell, C. W., & Klein,

S. A. (2016, August). Evidence for climate change in the satellite cloud record. *Nature*, *536*(7614), 72–75. Retrieved 2023-08-23, from https://www.nature.com/articles/nature18273 doi: 10.1038/nature18273

Qu, X., Hall, A., Klein, S. A., & DeAngelis, A. M. (2015, September). Positive tropical marine low-cloud cover feedback inferred from cloud-controlling factors. *Geophysical Research Letters*, *42*(18), 7767–7775. Retrieved 2021-03-28, from https://onlinelibrary.wiley.com/doi/10.1002/2015GL065627 doi: 10.1002/2015GL065627

Rasch, P. J., Xie, S., Ma, P., Lin, W., Wang, H., Tang, Q., . . . Yang, Y. (2019, August). An Overview of the Atmospheric Component of the Energy Exascale Earth System Model. *Journal of Advances in Modeling Earth Systems*, *11*(8), 2377–2411. Retrieved 2023-08-17, from https://onlinelibrary.wiley.com/doi/10.1029/2019MS001629 doi: 10.1029/2019MS001629

Rieck, M., Nuijens, L., & Stevens, B. (2012, August). Marine Boundary Layer Cloud Feedbacks in a Constant Relative Humidity Atmosphere. *Journal of the Atmospheric Sciences*, *69*(8), 2538–2550. Retrieved 2022-04-03, from https://journals.ametsoc.org/doi/10.1175/JAS-D-11-0203.1 doi: 10.1175/JAS-D-11-0203.1

Scott, R. C., Myers, T. A., Norris, J. R., Zelinka, M. D., Klein, S. A., Sun, M., & Doelling, D. R. (2020, September). Observed Sensitivity of Low-Cloud Radiative Effects to Meteorological Perturbations over the Global Oceans. *Journal of Climate*, *33*(18), 7717–7734. Retrieved 2022-07-28, from https://journals.ametsoc.org/view/journals/clim/33/18/jcliD191028.xml doi: 10.1175/JCLI-D-19-1028.1

Seager, R., & Henderson, N. (2013, October). Diagnostic Computation of Moisture Budgets in the ERA-Interim Reanalysis with Reference to Analysis of CMIP-Archived Atmospheric Model Data*. *Journal of Climate*, *26*(20), 7876–7901. Retrieved 2021-03-28, from http://journals.ametsoc.org/doi/10.1175/JCLI-D-13-00018.1 doi: 10.1175/JCLI-D-13-00018.1

Senior, C. A., & Mitchell, J. F. B. (1993, March). Carbon Dioxide and Climate. The Impact of Cloud Parameterization. *Journal of Climate*, *6*(3), 393–418. Retrieved 2023-02-22, from http://journals.ametsoc.org/doi/10.1175/1520-0442(1993)006<0393:CDACTI>2.0.CO;2 doi: 10.1175/1520-0442(1993)006⟨0393:CDACTI⟩2.0.CO;2

Shell, K. M., Kiehl, J. T., & Shields, C. A. (2008, May). Using the Radiative Kernel Technique to Calculate Climate Feedbacks in NCAR's Community Atmospheric Model. *Journal of Climate*, *21*(10), 2269–2282. Retrieved 2023-07-24, from http://journals.ametsoc.org/doi/10.1175/2007JCLI2044.1 doi: 10.1175/2007JCLI2044.1

Sherwood, S. C., Bony, S., & Dufresne, J.-L. (2014, January). Spread in model climate sensitivity traced to atmospheric convective mixing. *Nature*, *505*(7481), 37–42. Retrieved 2023-02-22, from http://www.nature.com/articles/nature12829 doi: 10.1038/nature12829

Sherwood, S. C., Webb, M. J., Annan, J. D., Armour, K. C., Forster, P. M., Hargreaves, J. C., . . . Zelinka, M. D. (2020, December). An Assessment of Earth's Climate Sensitivity Using Multiple Lines of Evidence. *Reviews of Geophysics*, *58*(4). Retrieved 2022-02-14, from https://onlinelibrary.wiley.com/doi/10.1029/2019RG000678 doi: 10.1029/2019RG000678

Siler, N., Roe, G. H., & Armour, K. C. (2018, September). Insights into the Zonal-Mean Response of the Hydrologic Cycle to Global Warming from a Diffusive Energy Balance Model. *Journal of Climate*, *31*(18), 7481–7493. Retrieved 2023-03-07, from https://journals.ametsoc.org/view/journals/clim/31/18/jcli-d-18-0081.1.xml doi: 10.1175/JCLI-D-18-0081.1

Slingo, J. M. (1980, October). A cloud parametrization scheme derived from GATE data for use with a numerical model. *Quarterly Journal of the Royal*

Meteorological Society, *106*(450), 747–770. Retrieved 2023-07-25, from `https://onlinelibrary.wiley.com/doi/10.1002/qj.49710645008` doi: 10.1002/qj.49710645008

Soden, B. J., Held, I. M., Colman, R., Shell, K. M., Kiehl, J. T., & Shields, C. A. (2008, July). Quantifying Climate Feedbacks Using Radiative Kernels. *Journal of Climate*, *21*(14), 3504–3520. Retrieved 2022-05-26, from `http://journals.ametsoc.org/doi/10.1175/2007JCLI2110.1` doi: 10.1175/2007JCLI2110.1

Sourdeval, O., C.-Labonnote, L., Baran, A. J., Mülmenstädt, J., & Brogniez, G. (2016, October). A methodology for simultaneous retrieval of ice and liquid water cloud properties. Part 2: Near-global retrievals and evaluation against A-Train products. *Quarterly Journal of the Royal Meteorological Society*, *142*(701), 3063–3081. Retrieved 2022-04-03, from `https://onlinelibrary.wiley.com/doi/10.1002/qj.2889` doi: 10.1002/qj.2889

Stephens, G. L. (1978, November). Radiation Profiles in Extended Water Clouds. II: Parameterization Schemes. *Journal of the Atmospheric Sciences*, *35*(11), 2123–2132. Retrieved 2023-08-24, from `http://journals.ametsoc.org/doi/10.1175/1520-0469(1978)035<2123:RPIEWC>2.0.CO;2` doi: 10.1175/1520-0469(1978)035⟨2123:RPIEWC⟩2.0.CO;2

Stephens, G. L., & Ellis, T. D. (2008, December). Controls of Global-Mean Precipitation Increases in Global Warming GCM Experiments. *Journal of Climate*, *21*(23), 6141–6155. Retrieved 2023-03-16, from `http://journals.ametsoc.org/doi/10.1175/2008JCLI2144.1` doi: 10.1175/2008JCLI2144.1

Stevens, B., & Brenguier, J.-L. (2009). *Cloud-controlling Factors.*

Storelvmo, T., & Tan, I. (2015, July). The Wegener-Bergeron-Findeisen process – Its discovery and vital importance for weather and climate. *Meteorologische Zeitschrift*, *24*(4), 455–461. Retrieved 2023-01-18, from `http://www.schweizerbart.de/papers/metz/detail/24/84731/The_Wegener_Bergeron_Findeisen_process__Its_discov?af=crossref` doi: 10.1127/metz/2015/0626

Storelvmo, T., Tan, I., & Korolev, A. V. (2015, December). Cloud Phase Changes Induced by CO2 Warming—a Powerful yet Poorly Constrained Cloud-Climate Feedback. *Current Climate Change Reports*, *1*(4), 288–296. Retrieved 2023-02-22, from `http://link.springer.com/10.1007/s40641-015-0026-2` doi: 10.1007/s40641-015-0026-2

Tan, I., Oreopoulos, L., & Cho, N. (2019, April). The Role of Thermodynamic Phase Shifts in Cloud Optical Depth Variations With Temperature. *Geophysical Research Letters*, *46*(8), 4502–4511. Retrieved 2023-04-10, from `https://onlinelibrary.wiley.com/doi/10.1029/2018GL081590` doi: 10.1029/2018GL081590

Tan, I., Storelvmo, T., & Zelinka, M. D. (2016, April). Observational constraints on mixed-phase clouds imply higher climate sensitivity. *Science*, *352*(6282), 224–227. Retrieved 2023-01-18, from `https://www.science.org/doi/10.1126/science.aad5300` doi: 10.1126/science.aad5300

Terai, C. R., Klein, S. A., & Zelinka, M. D. (2016, August). Constraining the low-cloud optical depth feedback at middle and high latitudes using satellite observations: CONSTRAINING LOW-CLOUD OPTICAL DEPTH FEEDBACK. *Journal of Geophysical Research: Atmospheres*, *121*(16), 9696–9716. Retrieved 2022-08-12, from `http://doi.wiley.com/10.1002/2016JD025233` doi: 10.1002/2016JD025233

Terai, C. R., Zhang, Y., Klein, S. A., Zelinka, M. D., Chiu, J. C., & Min, Q. (2019, February). Mechanisms Behind the Extratropical Stratiform Low-Cloud Optical Depth Response to Temperature in ARM Site Observations. *Journal of Geophysical Research: Atmospheres*, *124*(4), 2127–2147. Retrieved 2022-05-23, from `https://onlinelibrary.wiley.com/doi/10.1029/2018JD029359` doi:

10.1029/2018JD029359

Trenberth, K. (2011, March). Changes in precipitation with climate change. *Climate Research*, *47*(1), 123–138. Retrieved 2023-03-16, from `http://www.int-res.com/abstracts/cr/v47/n1-2/p123-138/` doi: 10.3354/cr00953

Tukey, J. W. (1958, June). Bias and Confidence in Not-quite Large Samples. (Abstracts of Papers). *The Annals of Mathematical Statistics*, *29*(2), 614. Retrieved 2023-04-06, from `http://projecteuclid.org/euclid.aoms/1177706647` doi: 10.1214/aoms/1177706647

Wall, C. J., Norris, J. R., Possner, A., McCoy, D. T., McCoy, I. L., & Lutsko, N. J. (2022, November). Assessing effective radiative forcing from aerosol–cloud interactions over the global ocean. *Proceedings of the National Academy of Sciences*, *119*(46), e2210481119. Retrieved 2023-01-26, from `https://pnas.org/doi/10.1073/pnas.2210481119` doi: 10.1073/pnas.2210481119

Webb, M. J., Lock, A. P., Bretherton, C. S., Bony, S., Cole, J. N. S., Idelkadi, A., ... Zhao, M. (2015, November). The impact of parametrized convection on cloud feedback. *Philosophical Transactions of the Royal Society A: Mathematical, Physical and Engineering Sciences*, *373*(2054), 20140414. Retrieved 2023-02-22, from `https://royalsocietypublishing.org/doi/10.1098/rsta.2014.0414` doi: 10.1098/rsta.2014.0414

Yettella, V., & Kay, J. E. (2017, September). How will precipitation change in extratropical cyclones as the planet warms? Insights from a large initial condition climate model ensemble. *Climate Dynamics*, *49*(5-6), 1765–1781. Retrieved 2023-02-05, from `http://link.springer.com/10.1007/s00382-016-3410-2` doi: 10.1007/s00382-016-3410-2

Zelinka, M. D., Grise, K. M., Klein, S. A., Zhou, C., DeAngelis, A. M., & Christensen, M. W. (2018, October). Drivers of the Low-Cloud Response to Poleward Jet Shifts in the North Pacific in Observations and Models. *Journal of Climate*, *31*(19), 7925–7947. Retrieved 2023-04-13, from `https://journals.ametsoc.org/doi/10.1175/JCLI-D-18-0114.1` doi: 10.1175/JCLI-D-18-0114.1

Zelinka, M. D., Klein, S. A., & Hartmann, D. L. (2012, June). Computing and Partitioning Cloud Feedbacks Using Cloud Property Histograms. Part II: Attribution to Changes in Cloud Amount, Altitude, and Optical Depth. *Journal of Climate*, *25*(11), 3736–3754. Retrieved 2022-05-26, from `https://journals.ametsoc.org/doi/10.1175/JCLI-D-11-00249.1` doi: 10.1175/JCLI-D-11-00249.1

Zelinka, M. D., Myers, T. A., McCoy, D. T., Po-Chedley, S., Caldwell, P. M., Ceppi, P., ... Taylor, K. E. (2020). *Causes of higher climate sensitivity in cmip6 models* (Vol. 47) (software No. 1). Wiley Online Library.

Zelinka, M. D., Myers, T. A., McCoy, D. T., Po-Chedley, S., Caldwell, P. M., Ceppi, P., ... Taylor, K. E. (2020, January). Causes of Higher Climate Sensitivity in CMIP6 Models. *Geophysical Research Letters*, *47*(1). Retrieved 2021-11-29, from `https://onlinelibrary.wiley.com/doi/abs/10.1029/2019GL085782` doi: 10.1029/2019GL085782

Zhai, C., Jiang, J. H., & Su, H. (2015, October). Long-term cloud change imprinted in seasonal cloud variation: More evidence of high climate sensitivity: Cloud Feedback and Seasonal Variation. *Geophysical Research Letters*, *42*(20), 8729–8737. Retrieved 2022-03-27, from `http://doi.wiley.com/10.1002/2015GL065911` doi: 10.1002/2015GL065911

Zhang, Y., Xie, S., Lin, W., Klein, S. A., Zelinka, M., Ma, P., ... Ma, H. (2019, May). Evaluation of Clouds in Version 1 of the E3SM Atmosphere Model With Satellite Simulators. *Journal of Advances in Modeling Earth Systems*, *11*(5), 1253–1268. Retrieved 2023-08-23, from `https://onlinelibrary.wiley.com/doi/10.1029/2018MS001562` doi: 10.1029/2018MS001562

Zhao, M. (2014, March). An Investigation of the Connections among Convection, Clouds, and Climate Sensitivity in a Global Climate Model. *Journal of Climate*, *27*(5), 1845–1862. Retrieved 2023-02-22, from http://journals.ametsoc.org/doi/10.1175/JCLI-D-13-00145.1 doi: 10.1175/JCLI-D-13-00145.1

Zheng, Y., Rosenfeld, D., & Li, Z. (2020, July). A More General Paradigm for Understanding the Decoupling of Stratocumulus-Topped Boundary Layers: The Importance of Horizontal Temperature Advection. *Geophysical Research Letters*, *47*(14), e2020GL087697. Retrieved 2023-08-24, from https://agupubs.onlinelibrary.wiley.com/doi/10.1029/2020GL087697 doi: 10.1029/2020GL087697

Figure 1.

Relationships between SW_{FB}, LWP Response ($\frac{\Delta LWP}{\Delta GMT}$), and Climate Sensitivity

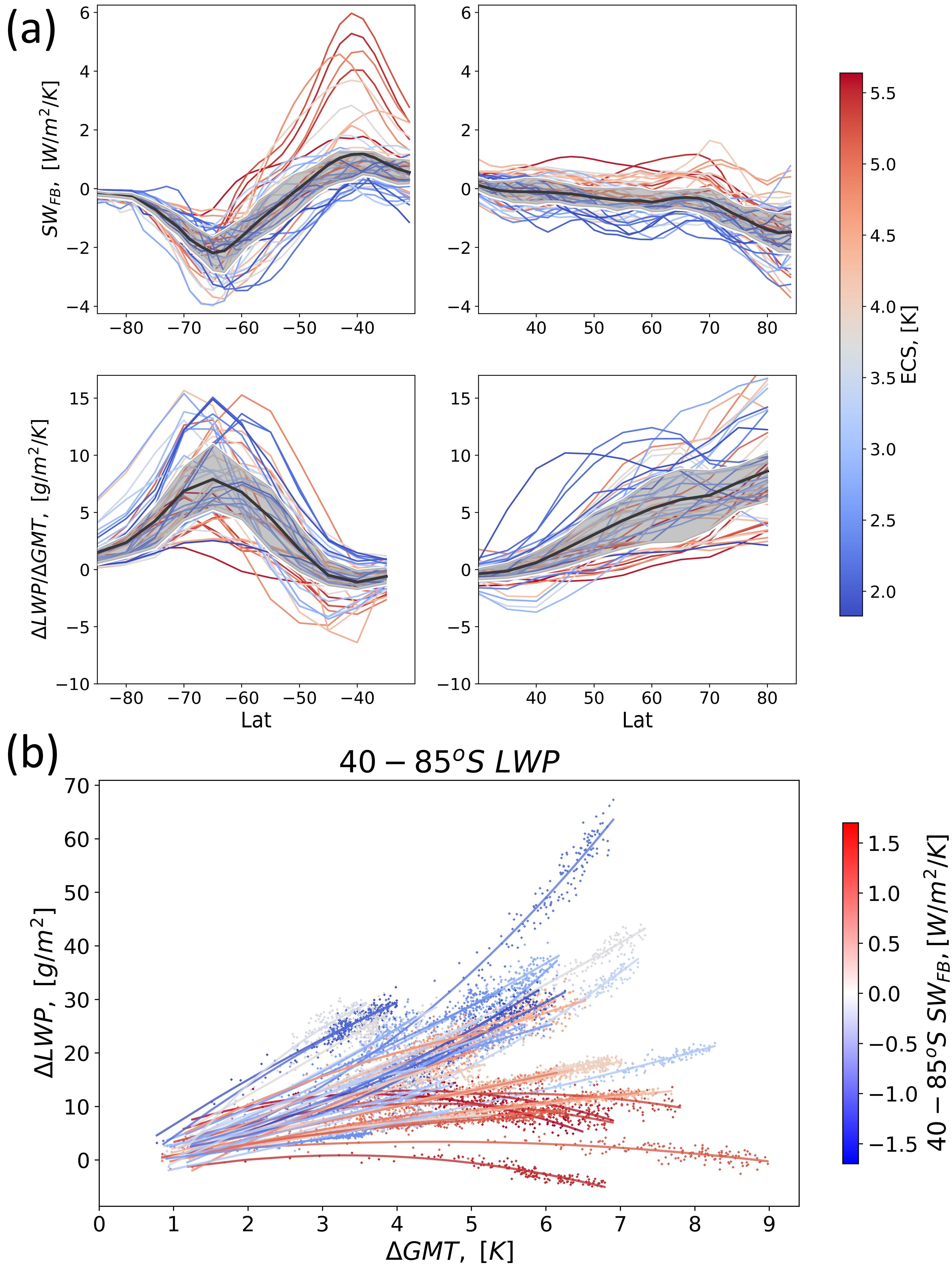

Figure 2.

Prediction of Observed LWP

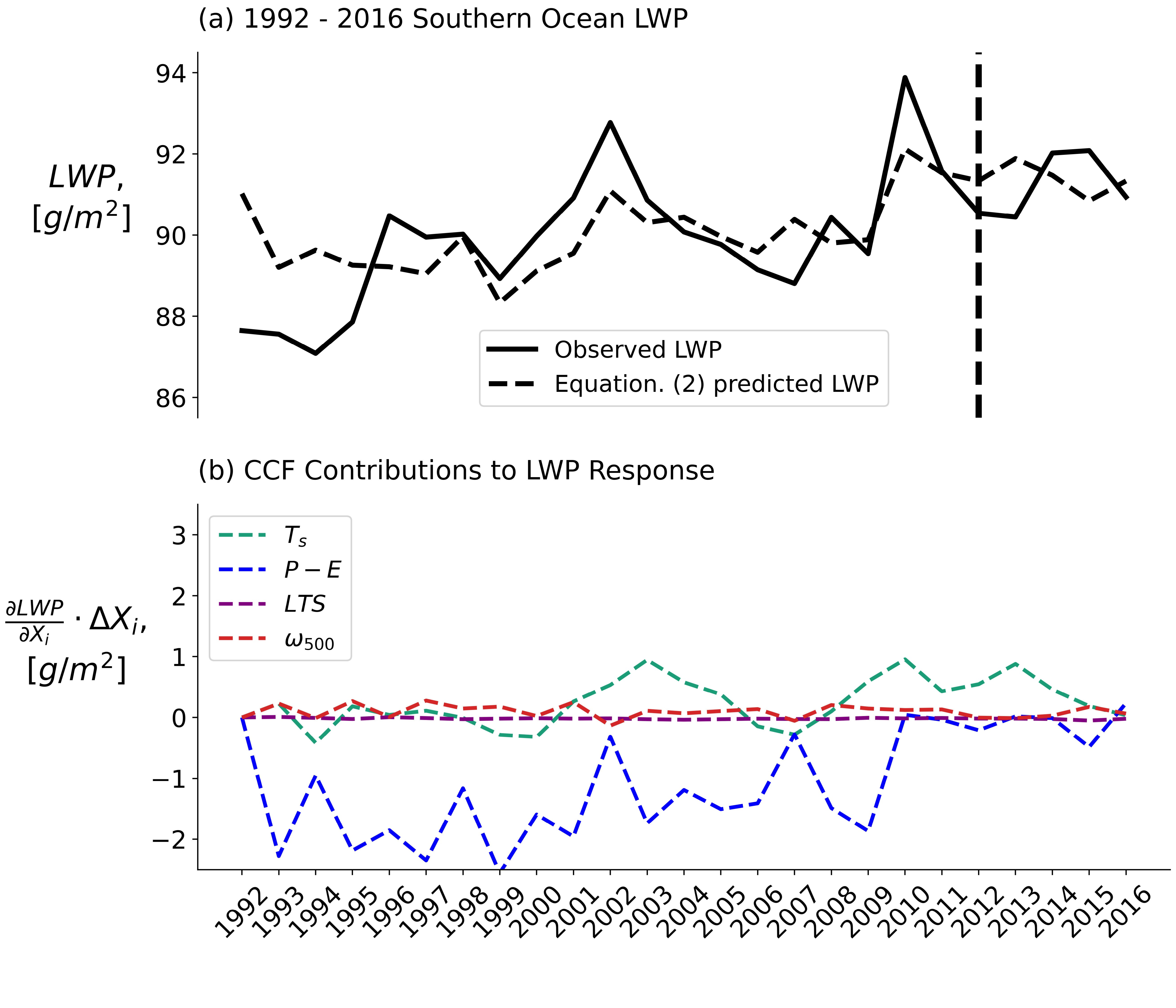

Figure 3.

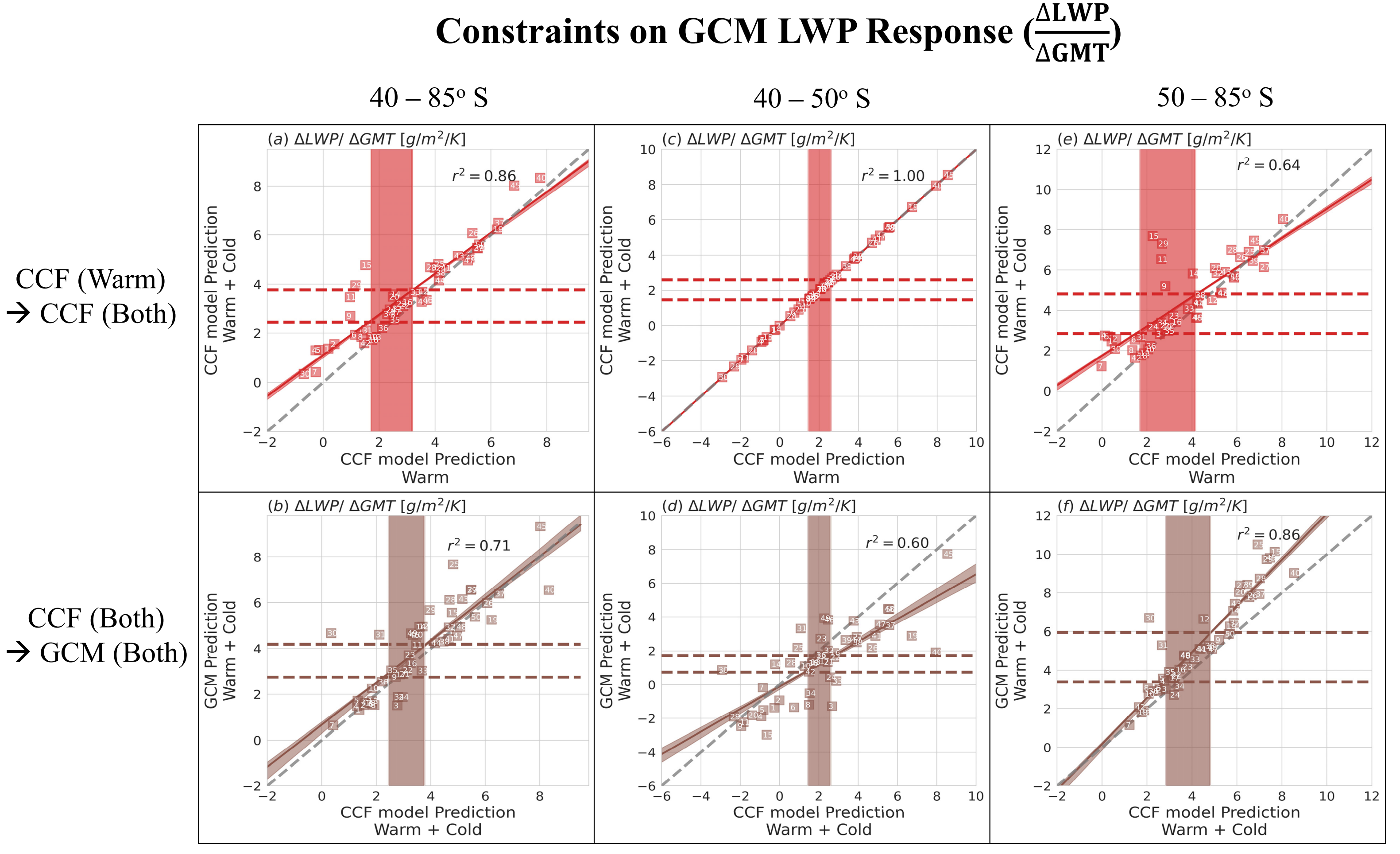

Constraints on GCM LWP Response (ΔLWP/ΔGMT)
40 – 85° S
40 – 50° S
50 – 85° S
CCF (Warm)
→ CCF (Both)
CCF (Both)
→ GCM (Both)
(a) ΔLWP/ ΔGMT [g/m²/K]
(b) ΔLWP/ ΔGMT [g/m²/K]
(c) ΔLWP/ ΔGMT [g/m²/K]
(d) ΔLWP/ ΔGMT [g/m²/K]
(e) ΔLWP/ ΔGMT [g/m²/K]
(f) ΔLWP/ ΔGMT [g/m²/K]
r² = 0.86
r² = 1.00
r² = 0.64
r² = 0.71
r² = 0.60
r² = 0.86
CCF model Prediction
Warm + Cold
CCF model Prediction
Warm
GCM Prediction
Warm + Cold

Figure 4.

Decomposition on LWP Response ($\frac{\Delta LWP}{\Delta GMT}$)

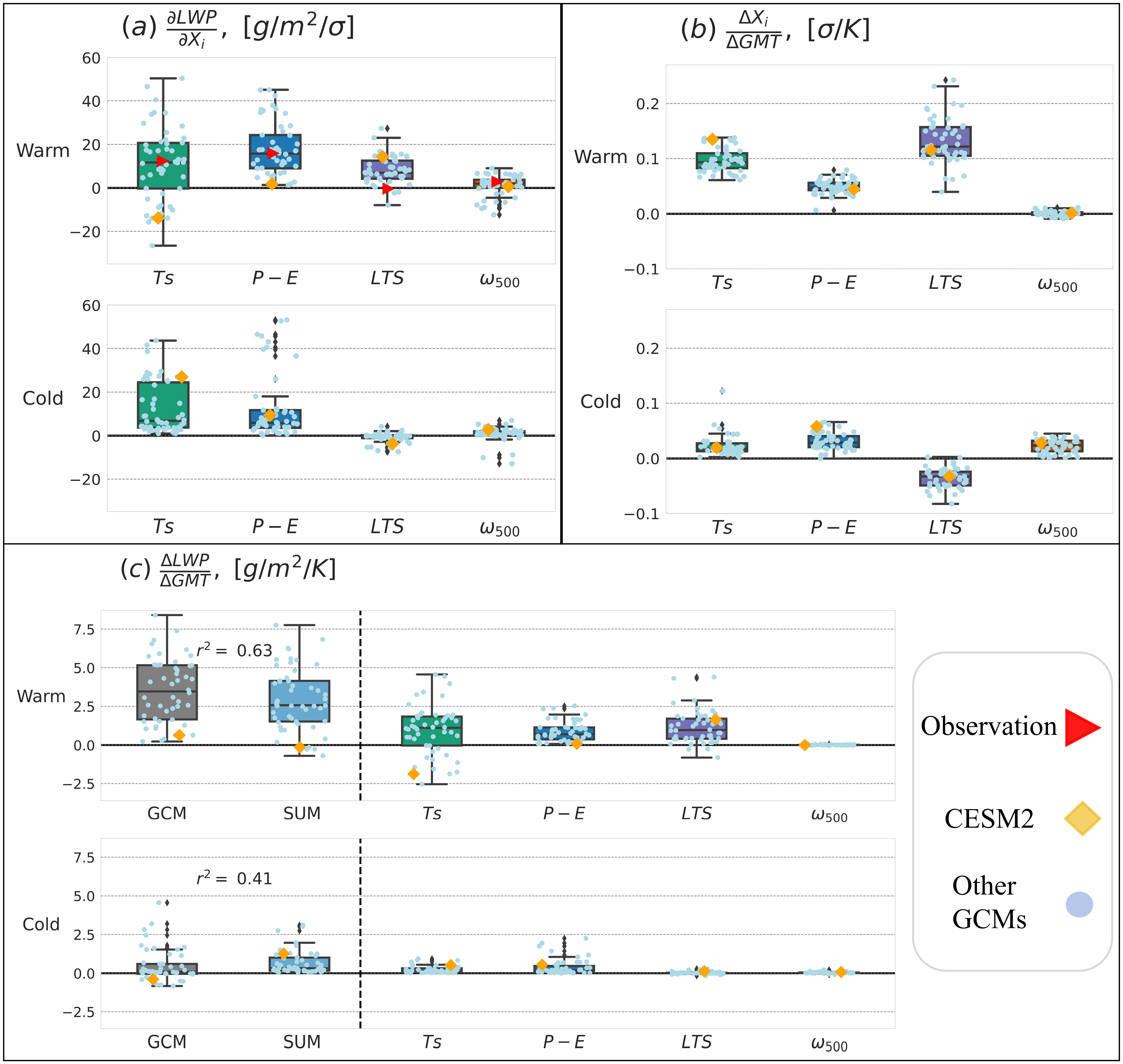

Figure 5.

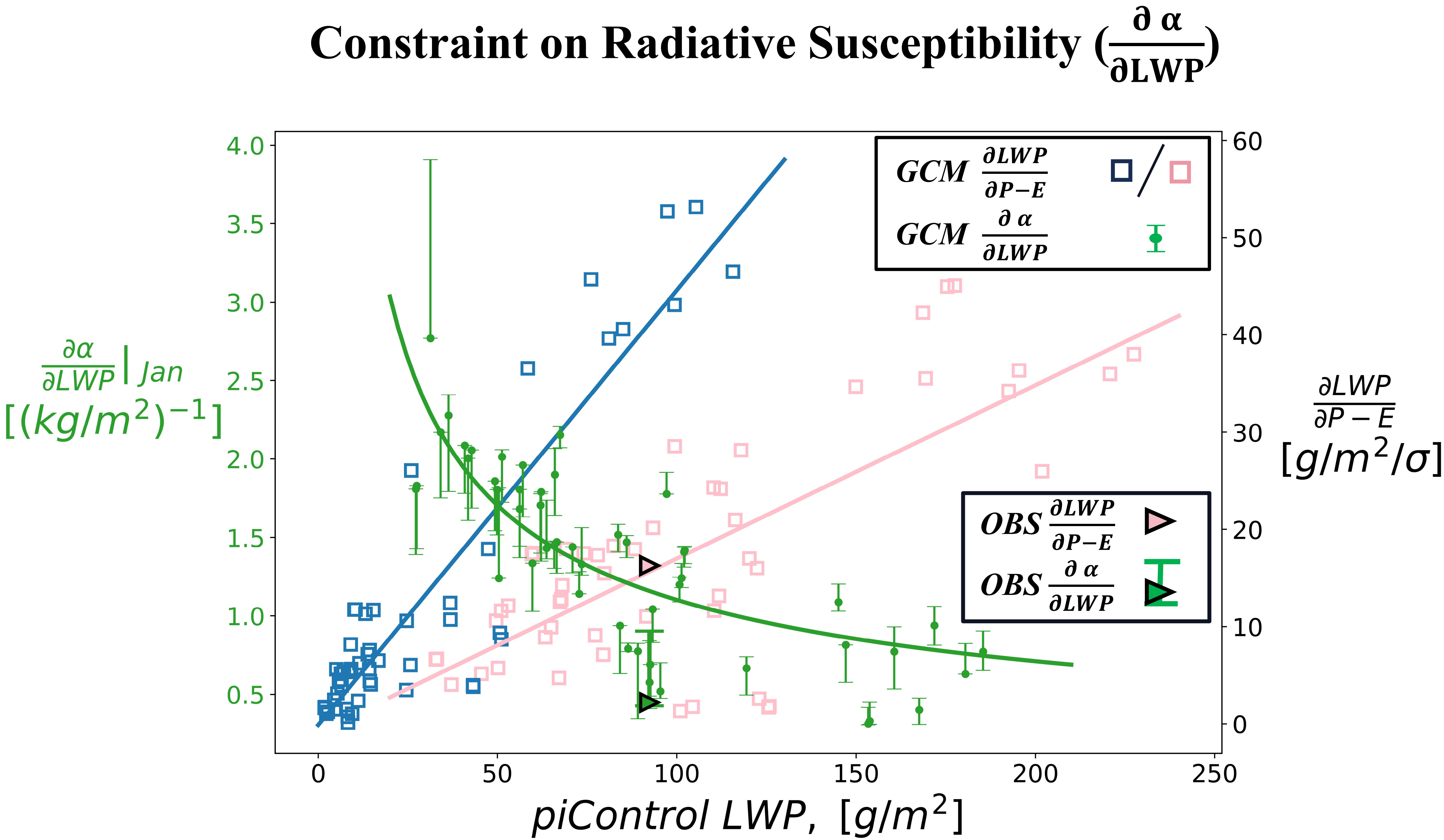

Constraint on Radiative Susceptibility ($\frac{\partial \alpha}{\partial LWP}$)
$\frac{\partial \alpha}{\partial LWP}|_{Jan}$ $[(kg/m^2)^{-1}]$
$\frac{\partial LWP}{\partial P-E}$ $[g/m^2/\sigma]$
piControl LWP, $[g/m^2]$
GCM $\frac{\partial LWP}{\partial P-E}$
GCM $\frac{\partial \alpha}{\partial LWP}$
OBS $\frac{\partial LWP}{\partial P-E}$
OBS $\frac{\partial \alpha}{\partial LWP}$
0.5
1.0
1.5
2.0
2.5
3.0
3.5
4.0
0
10
20
30
40
50
60
0
50
100
150
200
250

Figure 6.

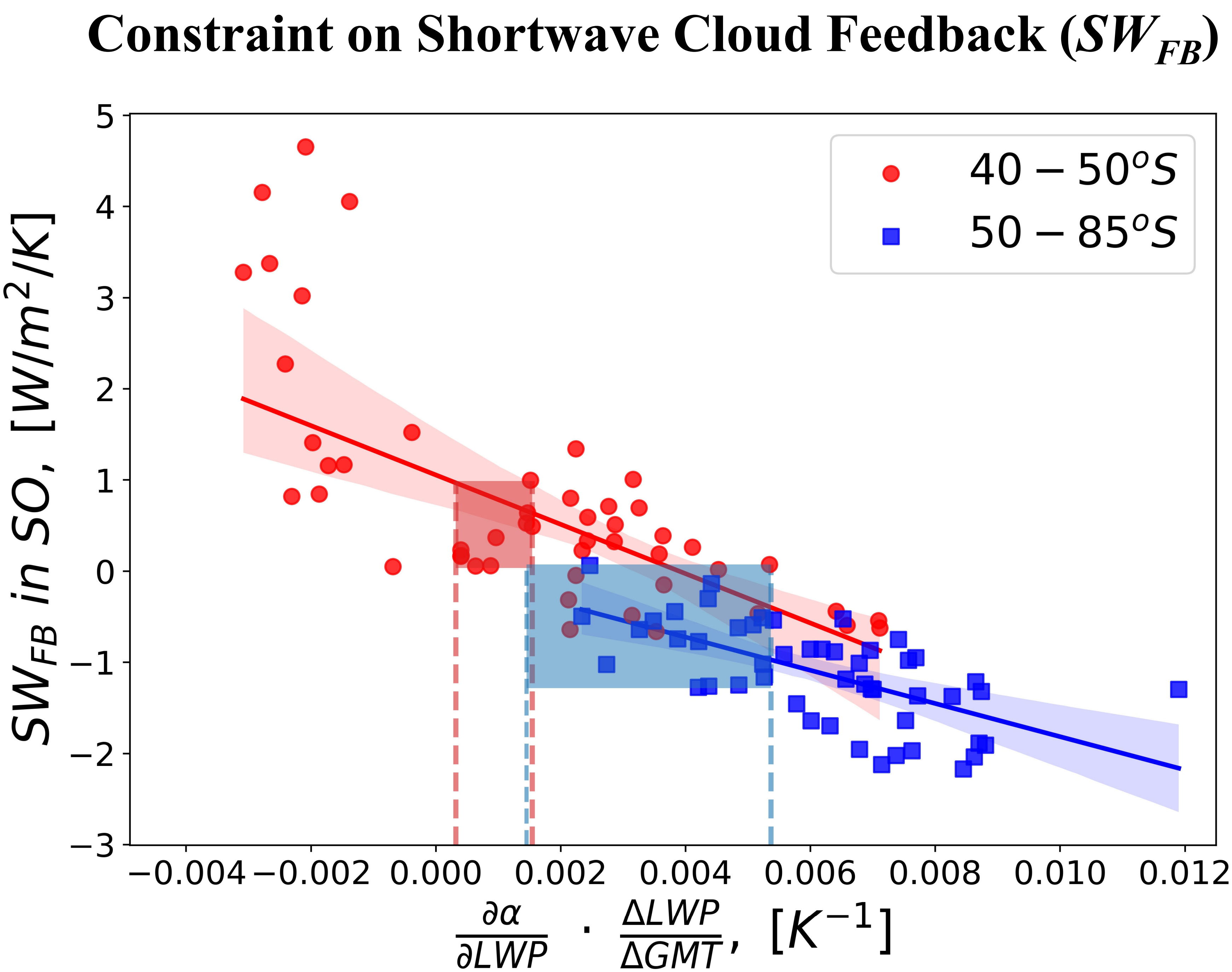

Constraint on Shortwave Cloud Feedback (SW_{FB})
SW_{FB} in SO, [$W/m^2/K$]
$\frac{\partial \alpha}{\partial LWP} \cdot \frac{\Delta LWP}{\Delta GMT}$, [$K^{-1}$]
$40-50^oS$
$50-85^oS$
5
4
3
2
1
0
−1
−2
−3
−0.004
−0.002
0.000
0.002
0.004
0.006
0.008
0.010
0.012

Figure 7.

GCM SW_{FB} prior
kde of SW_{FB}
Multimodel Mean
95% confidence interval of constraint
Number of GCMs
0
2
4
6
8
10
12
14
−0.4
−0.2
0.0
0.2
0.4
SW_{FB} $(40^o - 85^oS)$ $[W/m^2/K]$